Image Decomposition: Theory, Numerical Schemes, and Performance Evaluation

Jérôme Gilles

DGA/CEP - EORD department,
16bis rue Prieur de la Côte d'Or, 94110 Arcueil, France

Abstract

This paper describes the many image decomposition models that allow to separate structures and textures or structures, textures, and noise. These models combined a total variation approach with different adapted functional spaces such as Besov or Contourlet spaces or a special oscillating function space based on the work of Yves Meyer. We propose a method to evaluate the performance of such algorithms to enhance understanding of the behavior of these models.

Key words: image decomposition, *BV*, texture, noise, oscillating functions, Besov spaces, local adaptivity, contourlet spaces, soft thresholding, performance evaluation

Contents

Email address: `jerome.gilles@etca.fr` (Jérôme Gilles)
URL: `http://jerome.gilles91.free.fr` (Jérôme Gilles)

1. Introduction

In the last few years, different algorithms have been proposed to decompose an image into its structures and textures components and these ints structures, textures, and noise components. The initial idea was proposed by Meyer (2001). He proposed starting from the Rudin-Osher-Fatemi algorithm, (Rudin et al. (1992)), which was designed to perform image denoising. Meyer showed that this model rejects the textures and then proposed to use a new function space, G, by replacing the L^2-norm by the G-norm. He proved that this space corresponds to a space of oscillating functions that are useful to model textures. Two years later, two numerical schemes were proposed to solve Meyer's model, particularly the algorithm based on Chambolle's nonlinear projector. It is easy to implement, and convergence conditions are given by a theorem.

These models work well provided no noise is present in the image. Otherwise, it is necessary to extend the model to a three-part model. Different approachs were proposed based on a local adaptable algorithm or wavelet soft thresholding Aujol and Chambolle (2005); Gilles (2007b).

This paper describes the philosophy developped by Meyer and gives a description of the different structures + textures models in section 3 and structures + textures + noise models in section 4. A new three-part model, based on contourlet soft thresholding, is introduce. This mode improves the results of the previous algorithms.

Section 5 deals with performance evaluation of the decomposition algorithms. A specific methodology is proposed. First we create test images by recomposing structures, textures, and noise reference images that are generated separatly. We define some metrics to evaluate the quality of the different components obtained at the output of the decomposition algorithms (especially, the problem of how to measure the remaining residue in the noise).

Before detailing the different decomposition models, the first section provides some preliminaries and notations like the wavelet, contourlet formalism. It also presents the different function spaces and their associated norms that are used in the remainder of the paper.

We conclude by summarizing the different models and their performance. We also give some perspectives to this work.

2. Preliminaries

This section describes all the definitions used in the chapter. We start by recalling the multiresolution formalism, specially based on wavelets and other geometric approachs like curvelets and contourlets. We also introduce different function spaces like the space of bounded variations functions (BV), Besov spaces, and so on. We complete these descriptions by defining a space based on the contourlet expansion, which will be used in the new three-part decomposition model presented in section 4.3.

2.1. Wavelets

Let us start with the notations and properties of wavelet analysis. The first wavelet expansion of a one dimensional (1D) signal appeared in the 1980's (Härdle et al. (1997); Mallat (1999); Vidakovic and Mueller (1991)). The well-known contributors of the wavelet theory are, but not restricted to, Meyer (1993), Mallat (1999), and Daubechies (1992).

In the following, we assume that we have a 1D signal but the D-dimensional extension is naturally obtained by using D separable transforms along the different variables. Wavelet analysis outperforms the Fourier representation. Fourier transform decomposes a signal over a sine-cosine basis. This transform is well localized in frequency but not in time (sine and cosine functions are defined over an infinite domain). For example, if we analyze a transient phenomenon, its Fourier transform covers all the frequency plane while it is well localized in time. It is evident that a transform that is both localized in time and frequency is needed. The first solution used a windowed-Fourier transform. It allows decomposition of the time-frequency plane into many time-frequency atoms. However, this transform is not completely satisfactory because it does not authorize adaptable atoms. However we could be interested in analyzing many transient phenomena with different lengths, then adaptable atoms are necessary. The wavelet transform affords us this opportunity, and we now recall its definition.

2.1.1. Continuous Case

Wavelet transform decomposes a signal over a set of translated and dilated versions of a mother wavelet. A mother wavelet is a function $\psi \in L^2(\mathbb{R})$ that respects some criteria as follows:

$$\int_{\mathbb{R}} \psi(t)dt = 0 \qquad \text{zero mean,} \tag{1}$$

$$\|\psi\|_{L^2} = 1 \qquad \text{normalized,} \tag{2}$$

and ψ needs to be centered on 0. If we denote a and b as the dilation and translation parameters, respectively, then the set of wavelets is obtained from the mother wavelet ψ by

$$\psi_{a,b}(t) = \frac{1}{\sqrt{a}}\psi\left(\frac{t-b}{a}\right). \tag{3}$$

Then, we can define the wavelet transform of a function $f \in L^2(\mathbb{R})$ at time b and scale a by (ψ^* is the complex conjugate of ψ)

$$\mathcal{WT}_f(a,b) = \langle f, \psi_{a,b} \rangle = \int_{\mathbb{R}} f(t)\frac{1}{\sqrt{a}}\psi^*\left(\frac{t-b}{a}\right)dt. \tag{4}$$

It is easy to see that a wavelet transform can be written as a convolution product (denoted $\star$)

$$\mathcal{WT}_f(a,b) = f \star \bar{\psi}_a(b), \qquad \text{where} \quad \bar{\psi}_a(t) = \frac{1}{\sqrt{a}}\psi^*\left(\frac{-t}{a}\right). \tag{5}$$

The following theorem gives the conditions that permit reconstruction of the function f from its wavelet expansion.

Theorem 1 *Let $\psi \in L^2(\mathbb{R})$ be a real wavelet that respects the following admissibility condition:*

$$C_\psi = \int_0^{+\infty} \frac{|\hat{\psi}(\xi)|^2}{\xi}d\xi < +\infty, \tag{6}$$

where $\hat{\psi}$ is the Fourier transform of ψ. Then, all functions $f \in L^2(\mathbb{R})$ verify

$$f(t) = \frac{1}{C_\psi} \int_0^{+\infty} \int_{\mathbb{R}} \mathcal{WT}_f(a,b)\frac{1}{\sqrt{a}}\psi\left(\frac{t-b}{a}\right)db\frac{da}{a^2} \tag{7}$$

and (Parseval relation)

$$\int_{\mathbb{R}} |f(t)|^2dt = \frac{1}{C_\psi} \int_0^{+\infty} \int_{\mathbb{R}} |\mathcal{WT}_f(a,b)|db\frac{da}{a^2}. \tag{8}$$

A proof can be find in Mallat (1999).

Many papers in the literature deal with the choice of the mother wavelet ψ. According to the concerned applications, we can impose some complementary constraints to the wavelet (e.g. its regularity, the length of its support, the number of its zero moments).

2.1.2. Discrete Case

In practice, we have digital signals composed of N samples denoted $f[n]$. Let $\psi(t)$ be a continous wavelet where its support is $[-K/2, K/2]$; then the discrete wavelet, dilated by 2^j, is defined as

$$\psi_{jn}[k] = \frac{1}{\sqrt{2^j}}\psi[2^{-j}k - n]. \tag{9}$$

4

Then the discrete wavelet transform can be written as

$$\mathcal{WT}_f[n,j] = \sum_m f[m]\psi_{jn}^*[m] = \langle f, \psi_{jn}\rangle, \tag{10}$$

and the reconstruction formula is true if ψ has some complementary properties, (see Mallat (1999) for more details). Then, we have

$$f[m] = \sum_{j=0}^{+\infty} \sum_n \mathcal{WT}_f[n,j]\psi_{jn}[n]. \tag{11}$$

These relations show that filter banks, defined from ψ, can be used to implement the wavelet transform and its inverse.

2.2. Multiresolution Analysis

Multiresolution analysis is defined in Mallat (1999). Let $\{V_j\}_{j\in\mathbb{Z}}$ be a set of closed subspaces of $L^2(\mathbb{R})$. We said it is a multiresolution approximation if it meets the following conditions:

$$\forall (j,k) \in \mathbb{Z}^2 \ , \ f(t) \in V_j \Leftrightarrow f(t - 2^j k) \in V_j, \tag{12}$$

$$\forall j \in \mathbb{Z} \ , \ V_{j+1} \subset V_j, \tag{13}$$

$$\forall j \in \mathbb{Z} \ , \ f(t) \in V_j \Leftrightarrow f\left(\frac{t}{2}\right) \in V_{j+1}, \tag{14}$$

$$\lim_{j\to +\infty} V_j = \bigcap_{j=-\infty}^{+\infty} V_j = \{0\}, \tag{15}$$

$$\lim_{j\to -\infty} V_j = \overline{\bigcup_{j=-\infty}^{+\infty} V_j} = L^2(\mathbb{R}), \tag{16}$$

and there exists a function θ such that $\{\theta(t-n)\}_{n\in\mathbb{Z}}$ is a Riesz basis of V_0.

Let φ be a function (called the scale function) with its Fourier transform be defined by:

$$\hat{\varphi}(\omega) = \frac{\hat{\theta}(\omega)}{\left(\sum_{k=-\infty}^{+\infty} |\hat{\theta}(\omega + 2k\pi)|^2\right)^{1/2}}. \tag{17}$$

Then the set $\{\varphi_{jn}\}_{n\in\mathbb{Z}}$ defined by

$$\varphi_{jn}(t) = \frac{1}{\sqrt{2^j}}\varphi\left(\frac{t-n}{2^j}\right) \tag{18}$$

is an orthonormal basis of V_j. If we define $W_j = V_j \ominus V_{j+1}$, the wavelet set $\{\psi_{jn}\}_{n\in\mathbb{Z}}$ associated with φ (see Härdle et al. (1997); Mallat (1999); Vidakovic and Mueller (1991)

5

to learn to build such functions) is an orthonormal basis of W_j. Then all functions $f \in L^2(\mathbb{R})$ can be decomposed to

$$f(t) = \sum_n \alpha_n \varphi_{0n}(t) + \sum_{j=0}^{+\infty} \sum_n \beta_{jn} \psi_{jn}(t), \tag{19}$$

where the coefficients $\beta_{jn} = \langle f, \psi_{jn} \rangle$ are the wavelet transform coefficients and $\alpha_n = \langle f, \varphi_{0n} \rangle$ are the coefficients from the projection on the subspace V_0. In other terms, we have

$$(19) \iff f \in V_0 \oplus \bigoplus_{j=0}^{\infty} W_j. \tag{20}$$

2.3. Directional Multiresolution Analysis

The two dimensional (2D) extension of a wavelet generally uses the separability principle. It uses a 1D wavelet filter along the horizontal and vertical directions. In natural images, however, the information is not limited to these two directions. It is easy to understand that the multiresolution analysis needs to be extended to encompass directions in the image. Many authors propose different approachs to do this directional analysis. This chapter describes only those best known in the literature: the ridgelets, curvelets, and contourlets.

2.4. Ridgelets

In his doctoral dissertation, Candès (1998) proposes a new transform that deals with directionality in images: the ridgelet transform.

The ridgelets functions $\psi_{a,b,\theta}$ are defined in a manner similar to wavelets but add the notion of orientation (tuned by the θ parameter):

$$\psi_{a,b,\theta} : \mathbb{R}^2 \longrightarrow \mathbb{R}^2 \tag{21}$$

$$\psi_{a,b,\theta}(x_1, x_2) = \frac{1}{\sqrt{a}} \psi \left(\frac{x_1 \cos \theta + x_2 \sin \theta - b}{a} \right). \tag{22}$$

The $\psi_{a,b,\theta}$ is constant along the lines $x_1 \cos \theta + x_2 \sin \theta = c$ (c is a constant) and is a wavelet ψ in the orthogonal direction. Many properties of the wavelet theory can be transposed.

Definition 1. The admissibility condition for a ridgelet is:

$$K_\psi = \int \frac{\left| \hat{\psi}(\xi) \right|^2}{|\xi|^2} d\xi < \infty, \tag{23}$$

which is equivalent to $\int \psi(t) dt = 0$.

Morever, we assume that ψ is normalized:

$$\Rightarrow \int \frac{\left|\hat{\psi}(\xi)\right|^2}{|\xi|^2} d\xi = 1. \tag{24}$$

Under these assumptions, Candès defines the ridgelet transform of a function f by

Definition 2. For a function f, the coefficients of its ridgelet transform are given by

$$\mathcal{R}_f(a,b,\theta) = \int \psi_{a,b,\theta}^*(x_1,x_2) f(x_1,x_2) dx_1 dx_2 = < f, \psi_{a,b,\theta} >, \tag{25}$$

and the reconstruction formula is given by

$$f(x_1,x_2) = \int_0^{2\pi} \int_{-\infty}^{+\infty} \int_0^{+\infty} \mathcal{R}_f(a,b,\theta) \psi_{a,b,\theta}(x) \frac{da}{a^3} db \frac{d\theta}{4\pi}. \tag{26}$$

In addition, the Parseval relation is verified as in proposition 1 below,

Proposition 1 *If $f \in L^1 \cap L^2(\mathbb{R}^2)$ and if ψ is admissible, then*

$$\|f\|_{L^2}^2 = c_\psi \int |\langle f, \psi_{a,b,\theta}\rangle|^2 \frac{da}{a^3} db \frac{d\theta}{4\pi}, \tag{27}$$

where $c_\psi = (4\pi)^{-1} K_\psi^{-1}$.

The proof can be found in Candès (1998).

In pratice, the ridgelet transform can be implemented by using the Radon transform and the 1D wavelet transform (see Candès (1998) for more details).

2.5. Curvelets

From the definition of the ridgelet transform, it is easy to see that this transform is a global transform (we mean that it is efficient to represent lines that go through the entire image). But images contain more general edges that are present locally. Candès and Donoho (1999); Candès et al. (2005); Donoho and Duncan (1999) propose a new approach that provides a local directional multiresolution analysis called the curvelet transform.

The idea is to do a specific tiling of the space and frequency planes by using two windows, the radial window $W(r)$ and the angular window $V(t)$, where (r,θ) are the polar coordinates in the frequency plane and $r \in (1/2, 2)$. The window V is defined for $t \in [-1,1]$. These windows obey the following admissibility conditions:

$$\sum_{j=-\infty}^{+\infty} W^2(2^j r) = 1 \qquad r \in (3/4, 3/2) \tag{28}$$

and

$$\sum_{l=-\infty}^{+\infty} V^2(t-l) = 1 \qquad t \in (-1/2, 1/2) \tag{29}$$

7

Then for each $j \geqslant j_0$, a frequency window U is defined in the Fourier domain by

$$U_j(r, \theta) = 2^{-3j/4} W(2^{-j} r) V\left(\frac{2^{\lfloor j/2 \rfloor} \theta}{2\pi}\right), \tag{30}$$

where $\lfloor j/2 \rfloor$ is the integer part of $j/2$. Let $\varphi_j(x)$ denote the function such that its Fourier transform $\hat{\varphi}_j(\omega) = U_j(w)$ ((r, θ) are the polar coordinates corresponding to $w = (w_1, w_2)$). Then we define at scale 2^{-j}, orientation θ_l, and position $x_k^{(j,l)}$ a set of curvelets by

$$\varphi_{j,l,k}(x) = \varphi_j\left(R_{\theta_l}(x - x_k^{(j,l)})\right), \tag{31}$$

where R_{θ_l} is the rotation by θ_l radians. Then the curvelet transform is simply defined by the inner product between a function $f \in \mathbb{R}^2$ with the set of curvelets. A curvelet coefficient can be written

$$c(j, l, k) = \langle f, \varphi_{j,l,k} \rangle = \int_{\mathbb{R}^2} f(x) \varphi_{j,l,k}^*(x) dx. \tag{32}$$

More details can be found in Candès et al. (2005). In their paper, the authors prove the following proposition.

Proposition 2 *Let $f \in L^2(\mathbb{R}^2)$ denote a function expanded over a set of curvelets $\varphi_{j,l,k}$; we have the following reconstruction formula:*

$$f = \sum_{j,l,k} \langle f, \varphi_{j,l,k} \rangle \varphi_{j,l,k} \qquad \text{(Tight frame,)} \tag{33}$$

and the Parseval relation is verified:

$$\sum_{j,l,k} |\langle f, \varphi_{j,l,k} \rangle|^2 = \|f\|_{L^2}^2, \qquad \forall f \in L^2(\mathbb{R}^2). \tag{34}$$

All details about the numerical aspects can be found in Candès et al. (2005).

2.6. Contourlets

In 1999, when Candès et al. proposed the curvelet transform, the authors showed many promising results. The main drawback of the first version of curvelets is the difficulty of its numerical implementation (the discrete curvelet transform was proposed in 2005 Candès et al. (2005)). In order to "overcome" this problem, Do (2001, 2003); Do and Vetterli (2001, 2002, 2003a,b); Po and Do (2006) proposed a new algorithm, called the contourlet transform, initially designed in a discrete framework. The idea is to combine a multiscale decomposition and directional filtering at each scale (Figure 1).

The multiscale decomposition is obtained by using a Laplacian pyramid decomposition (LP) (Burt and Adelson (1983)). The directional filtering uses a directional filter bank (DFB) based on quincunx filters (Bamberger and Smith (1992)). In the next theorem, the authors show that this transform produces a tight frame.
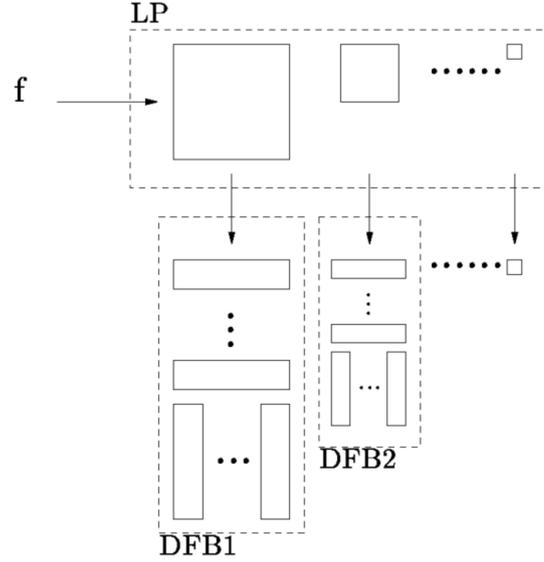
8

Figure 1: Contourlet transform principle.

Theorem 2 *Let j be the scale, n the position, $\{l_j\}_{j \leqslant j_0}$ the set of number of directions for each scale j. Then, the set*

$$\left\{ \phi_{j_0,n}(t); \rho_{j,k,n}^{(l_j)}(t) \right\}_{j \leqslant j_0,\, 0 \leqslant k \leqslant 2^{l_j}-1,\, n \in \mathbb{Z}^2} \tag{35}$$

is a tight frame of $L_2(\mathbb{R}^2)$.

All details about the construction of functions $\phi_{j_0,n}(t)$ and $\rho_{j,k,n}^{(l_j)}(t)$ can be found in Do (2001).

This implies

Corollary 1

$$f(t) = \sum_n \alpha_n \phi_{j_0,n}(t) + \sum_{j \leqslant j_0} \sum_{k=0}^{2^{l_j}-1} \sum_n \beta_{j,k,n} \rho_{j,k,n}^{(l_j)}(t) \tag{36}$$

or

$$f(t) = \sum_{j \in \mathbb{Z}} \sum_{k=0}^{2^{l_j}-1} \sum_n \beta_{j,k,n} \rho_{j,k,n}^{(l_j)}(t), \tag{37}$$

where $\alpha_n = \langle f | \phi_{j_0,n} \rangle$ and $\beta_{j,k,n} = \langle f | \rho_{j,k,n}^{(l_j)} \rangle$ are the contourlet transform coefficients.

9

2.7. Function Spaces

In Sections 3 and 4, we will use some function spaces and more particularly their associated norms. This section briefly describes the spaces of interest (it is assumed that the reader knows the L^p spaces and d is the dimension). The goal of the different spaces is to characterize some properties like the differentiability and the regularity of functions.

2.7.1. Sobolev Spaces

The first spaces we are interested in are the Sobolev spaces $W^{k,p}$. These spaces are defined as the spaces of functions f such that they and their weak derivatives up to some order k have a finite L^p norm, for a given $p \geqslant 1$. These spaces are endowed with the following norm:

$$\|f\|_{W^{k,p}} = \left(\sum_{i=0}^{k} \|f^{(i)}\|_{L^p}^p \right)^{1/p} = \left(\sum_{i=0}^{k} \int |f^{(i)}(t)|^p dt \right)^{1/p}. \tag{38}$$

An interesting particular case is for $p = 2$, denoted $H^k = W^{k,2}$, because of their relation with the Fourier series. More information about the Sobolev spaces can be found in the book by Adams (1975).

2.7.2. Besov Spaces

The next kind of spaces are Besov spaces $B_{p,q}^s$. Functions taken in $B_{p,q}^s$ have s derivatives in L^p. The parameter q permits more precise characterization of the regularity. A general description of these spaces can be found in Triebel (1992). In this paper, we give only their connection with wavelets. Indeed, different expressions exists for the norm associated with Besov space but one uses the wavelet coefficients, see (39).

$$\forall f \in B_{p,q}^s \qquad \|f\|_{B_{p,q}^s} = \left[\sum_n |\alpha_n|^p \right]^{1/p}$$
$$+ \left(\sum_{j=0}^{+\infty} 2^{j\left(\frac{d}{2}-\frac{1}{p}+s\right)q} \left[\sum_n 2^{j\frac{p}{2}} |\beta_{jn}|^p \right]^{q/p} \right)^{1/q}. \tag{39}$$

The homogeneous version is

$$\forall f \in \dot{B}_{p,q}^s \qquad \|f\|_{\dot{B}_{p,q}^s} = \left(\sum_{j=-\infty}^{+\infty} 2^{j\left(\frac{d}{2}-\frac{1}{p}+s\right)q} \left[\sum_n 2^{j\frac{p}{2}} |\beta_{jn}|^p \right]^{q/p} \right)^{1/q}, \tag{40}$$

where α_n and β_{jn} are the coefficients issued from the wavelet expansion (see Section 2.2).

2.7.3. Ridgelet Spaces

In the same way as previous, Candès define the ridgelet spaces $R_{p,q}^s$ endowed with the norm based on the ridgelet coefficients.

Definition 3. For $s \geqslant 0$ and $p, q > 0$, we said that $f \in R_{p,q}^s$ if $f \in L^1$ and

$$\underset{u}{Ave} \|R_f(u,.) \star \varphi\|_{L^p} < \infty$$

$$\text{and} \quad \left\{ 2^{js} 2^{j(d-1)/2} \left(\underset{u}{Ave} \|R_f(u,.) \star \psi_j\|_{L^p}^p \right)^{1/p} \right\} \in l_q(\mathbb{N}), \quad (41)$$

where $R_f(u,t) = \int_{u.x=t} f(x)dx$ is the Radon transform of f ($u = (\cos\theta; \sin\theta)$). The function φ is the scale function associated with ψ.

Then the induced norm is defined by

$$\|f\|_{R_{p,q}^s} = \underset{u}{Ave} \|R_f(u,.) \star \varphi\|_{L^p}$$

$$+ \left\{ \sum_{j \geqslant 0} \left(2^{js} 2^{j(d-1)/2} \left(Ave_u \|R_f(u,.) \star \psi_j\|_{L^p}^p \right)^{1/p} \right)^q \right\}^{1/q} \quad (42)$$

and its homogeneous version $\dot{R}_{p,q}^s$

$$\|f\|_{\dot{R}_{p,q}^s} = \left\{ \sum_{j \in \mathbb{Z}} \left(2^{js} 2^{j(d-1)/2} \left(Ave_u \|R_f(u,.) \star \psi_j\|_{L^p}^p \right)^{1/p} \right)^q \right\}^{1/q}. \quad (43)$$

As in the Besov case, these norms can be calculated from the ridgelet coefficients. Let $w_j(u,b)(f) = \langle f(x), \psi_j(u.x - b) \rangle$ for $j \geqslant 0$ and $v(u,b)(f) = \langle f(x), \varphi(u.x - b) \rangle$ these ridgelet coefficients, then

$$\|f\|_{R_{p,q}^s} = \left(\int |v(u,b)(f)|^p dudb \right)^{1/p}$$

$$+ \left\{ \sum_{j \geqslant 0} \left(2^{js} 2^{j(d-1)/2} \left(\int |w_j(u,b)(f)|^p dudb \right)^{1/p} \right)^q \right\}^{1/q}. \quad (44)$$

More information can be found in Candès (1998).

2.7.4. Contourlet Spaces

Inspired from the previous spaces, we propose to define the contourlet spaces, which will be denoted $Co_{p,q}^s$.

Definition 4. Let $s \geqslant 0$ and $p, q > 0$, if $f \in Co_{p,q}^s$; then

$$\|f\|_{Co_{p,q}^s} = \left[\sum_n |\alpha_{j_0,n}|^p \right]^{1/p}$$

$$+ \left\{ \sum_{j \leqslant j_0} 2^{j\left(\frac{d}{2} - \frac{1}{p} + s\right)q} \left[\sum_{k=0}^{2^{l_j}-1} \sum_n 2^{j\frac{p}{2}} |\beta_{j,k,n}|^p \right]^{q/p} \right\}^{1/q}, \quad (45)$$

or in the homogeneous case,

$$\|f\|_{\dot{C}o^s_{p,q}} = \left\{ \sum_{j\in\mathbb{Z}} 2^{j\left(\frac{d}{2} - \frac{1}{p} + s\right)q} \left[\sum_{k=0}^{2^{l_j}-1} \sum_n 2^{j\frac{p}{2}} |\beta_{j,k,n}|^p \right]^{q/p} \right\}^{1/q}, \tag{46}$$

where $\alpha_{j_0,n}$ and $\beta_{j,k,n}$ are the contourlet coefficients mentioned in Section 2.6.

2.7.5. Bounded Variation (BV) Spaces

The last space of interest is the BV space, the space of bounded variations functions. This space is widely used in image processing because it is a good candidate to modelize structures in images.

Definition 5. The space BV over a domain Ω is defined as

$$BV = \left\{ f \in L^1(\Omega); \int_\Omega |\nabla f| < \infty \right\}, \tag{47}$$

where ∇f is the gradient, in the distributional sense, of f and

$$\int_\Omega |\nabla f| = \sup_{\overrightarrow{\varphi}} \left\{ \int_\Omega f \operatorname{div} \overrightarrow{\varphi}; \qquad \overrightarrow{\varphi} \in C_0^1(\Omega, \mathbb{R}^2), |\overrightarrow{\varphi}| \leqslant 1 \right\}. \tag{48}$$

This space is endowed with the following norm:

$$\|f\|_{BV} = \|f\|_{L^1} + \int_\Omega |\nabla f|. \tag{49}$$

But in general, we only keep the second term, which is well known as the total variation of f. In the rest of the paper, we will use the notation

$$J(f) = \int_\Omega |\nabla f|. \tag{50}$$

More information about the BV space is available in Haddad (2005); Vese (1996).

We now have all the basic tools needed to describe the image decomposition models. The next two sections present the structures + textures and structures + textures + noise models, respectively.

3. Structures + Textures Decomposition

The starting point of the image decomposition models is the work of Meyer (2001) about the Rudin-Osher-Fatemi (ROF) algorithm (Rudin et al. (1992)). Let us recall the ROF model. Assume f is an observed image that is the addition of the ideal scene image u, which we want to retrieve, and a noise b. The authors propose to minimize the following functional to get u:

$$F_\lambda^{ROF}(u) = J(u) + \lambda \|f - u\|_{L^2}^2. \tag{51}$$

This model assumes that u is in BV because this space preserves sharp edges. This algorithm gives good results and is very easy to implement by using the nonlinear projectors proposed by Chambolle (2004) (see Appendix A).

Now if we take the image decomposition point of view, $f = u + v$, the functional in Eq.(51) can be rewritten as

$$F_\lambda^{ROF}(u,v) = J(u) + \lambda \|v\|_{L^2}^2. \tag{52}$$

We remind the reader that decomposition means u is the structures part and v the textures part. Meyer shows that this model is not adapted to achieve this decomposition. In order to convince us, the following example illustrates that the more a texture is oscillating, the more it is removed from both the u and v parts.

Example 1. Let v be a texture created from an oscillating signal over a finite domain. Then v can be written ($x = (x_1, x_2)$) as follows:

$$v(x) = \cos(\omega x_1)\theta(x), \tag{53}$$

where ω is the frequency and θ the indicator function over the considered domain. Then we can calculate the L^2 and BV norms of v, respectively. We get

$$\|v\|_{L^2} \approx \frac{1}{\sqrt{2}} \|\theta\|_{L^2}, \tag{54}$$

which is constant $\forall \omega$ and does not specially capture textures. In addition,

$$\|v\|_{BV} = \frac{\omega}{2\pi} \|\theta\|_{L^1}, \tag{55}$$

which grows as $\omega \to \infty$ and then clearly rejects textures.

In order to adapt the ROF model to capture the textures in the v component, Meyer proposes to replace L^2 space by another space, called G, which is a space of oscillating functions. He proves that this space is the dual space of $\mathcal{BV}$ (where $\mathcal{BV} = \{f \in L^2(\mathbb{R}^2)$, $\nabla f \in L^1(\mathbb{R}^2)\}$, which is close to the BV space and the total variation described earlier in the paper); see Meyer (2001) for more theoretical details about these spaces.

This space G is endowed by the following norm:

$$\|v\|_G = \inf_g \left\| \left(|g_1|^2 + |g_2|^2 \right)^{\frac{1}{2}} \right\|_{L^\infty}, \tag{56}$$

where $g = (g_1, g_2) \in L^\infty(\mathbb{R}^2) \times L^\infty(R^2)$ and $v = \operatorname{div} g$. If we calculate the G-norm of the oscillating texture in Eq.(53) of example 1, we get

$$\|v\|_G \leqslant \frac{C}{|\omega|}, \tag{57}$$

where C is a constant. Then it is easy to see that this space G is well adapted to capture textures. Now, the modified functional performing the structures + textures decomposition is

13

$$F_\lambda^{YM}(u,v) = J(u) + \lambda\|v\|_G, \tag{58}$$

where $f = u + v$, $f \in G$, $u \in BV$, $v \in G$. The drawback of this model is the presence of an L^∞ norm in the the expression of the G-norm (this does not allow classic variational calculus).

The first people who proposed a numerical algorithm to solve the Meyer model were Vese and Osher (2002). Their approach was to use the theorem which tells that $\forall f \in L^\infty(\Omega), \|f\|_{L^\infty} = \lim_{p\to\infty}\|f\|_{L^p}$ and a slightly modified version of Meyer's functional:

$$F_{\lambda,\mu,p}^{OV}(u,g) = J(u) + \lambda\|f - (u + \operatorname{div}\ g)\|_{L^2}^2 + \mu\left\|\sqrt{g_1^2 + g_2^2}\right\|_{L^p}. \tag{59}$$

Then variational calculus applies and results in a system of three connected partial differential equations. All the details of the equations discretization are available in Vese and Osher (2002). This algorithm works well but is very sensitive in the choice of its parameters, which induced many instability.

Another way to solve Meyer model was proposed by Aujol (2004); Aujol et al. (2003, 2006). The authors propose a dual-method approach that naturally arises because of the dual relation between the G and BV spaces. The problem is assumed to be in the discrete case and defined over a finite domain Ω. They proposed a modified functional to minimize.

$$F_{\lambda,\mu}^{AU}(u,v) = J(u) + J^*\left(\frac{v}{\mu}\right) + (2\lambda)^{-1}\|f - u - v\|_{L^2}^2 \tag{60}$$

and

$$(u,v) \in BV(\Omega) \times G_\mu(\Omega). \tag{61}$$

The set G_μ is the subset in G where $\forall v \in G_\mu$, $\|v\|_G \leqslant \mu$. Moreover, J^* is the characteristic function over G_1 with the property that J^* is the dual operator of J ($J^{**} = J$). Thus,

$$J^*(v) = \begin{cases} 0 & \text{if } v \in G_1 \\ +\infty & \text{else.} \end{cases} \tag{62}$$

The interesting point is that the precited Chambolle's projectors are the projector over the sets $G_\mu, \forall\mu$; these operators will be denoted P_{G_μ} in the rest of the paper. More details about these projectors can be found in Chambolle (2004) and recalled in Appendix A. Then the authors propose an iterative algorithm that gives the minimizers $(\hat{u},\hat{v})$ of $F_{\lambda,\mu}^{AU}(u,v)$.

- Let us fix v, we seek for the minimizer u of

$$\inf_u\left(J(u) + (2\lambda)^{-1}\|f - u - v\|_{L^2}^2\right). \tag{63}$$

- Now we fix u and seek for the minimizer v of

$$\inf_v J^*\left(\frac{v}{\mu}\right) + \|f - u - v\|_{L^2}^2. \tag{64}$$

14

Chambolle's results show that the solution of Eq.(63) is given by

$$\hat{u} = f - \hat{v} - P_{G_\lambda}(f - \hat{v}) \tag{65}$$

and the solution of Eq. (64) by

$$\hat{v} = P_{G_\mu}(f - \hat{u}). \tag{66}$$

Then the numerical algorithm is

1. Initialization:
$$u_0 = v_0 = 0$$

2. Iteration $n + 1$:

$$v_{n+1} = P_{G_\mu}(f - u_n)$$
$$u_{n+1} = f - v_{n+1} - P_{G_\lambda}(f - v_{n+1})$$

3. We stop the algorithm if

$$\max\left(|u_{n+1} - u_n|, |v_{n+1} - v_n|\right) \leqslant \epsilon$$

or if we reach a prescribed maximal number of iterations.

The authors prove that the minimizers $(\hat{u}, \hat{v})$ are also minimizers of the original Meyer functional Eq. (58), and that it is better to start by calculating v_{n+1} than u_{n+1}. See Aujol (2004); Aujol et al. (2003) for the complete proofs.

Figure 2 presents the three original images (Barbara, House, and Leopard) use for tests in the rest of the paper. Figures 3, 4, and 5 illustrate the results from Aujol's algorithm. The chosen parameters are $(\lambda = 1, \mu = 100)$, $(\lambda = 10, \mu = 1000)$, and $(\lambda = 5, \mu = 1000)$ respectively. For clarity reasons, we enhanced the contrasts of the textured components. On each test we see that the separation between structures and textures works well. Some residual textures remain in the structures part; this can be explained by the fact the parameter λ acts as a tradeoff between the "power" of separability and too much regularization of u.

As the G-norm is difficult to handle, Meyer (2001) proposes to replace the space G by the Besov space $\dot{B}_{-1,\infty}^\infty$ because $G \subset \dot{B}_{-1,\infty}^\infty$ (in the following, we will denote $E = \dot{B}_{-1,\infty}^\infty$). The advantage is that the norm of a function v over this space can be defined from its wavelet coefficients. The corresponding model proposed by Meyer is
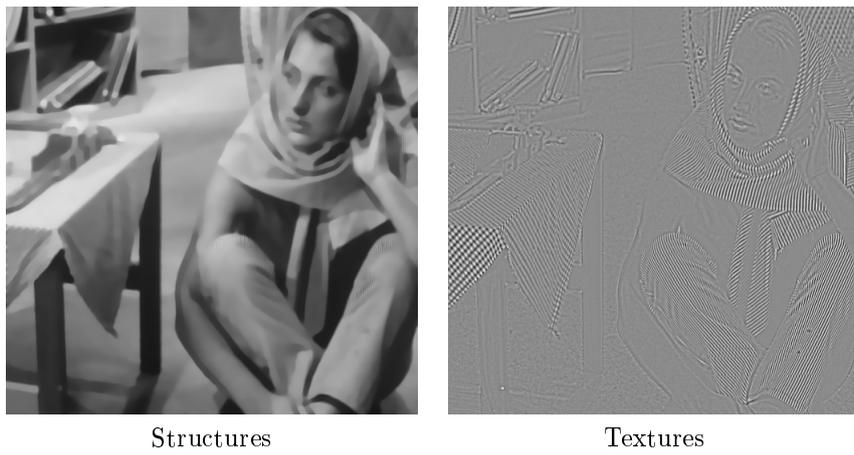
$$F_\lambda^{YM2}(u, v) = J(u) + \lambda\|v\|_E \tag{67}$$

Aujol and Chambolle were the first to propose a numerical algorithm that uses the space E. As previously, they reformulated the model in a dual-method approach, where E_μ is the subset of E, where $\forall f \in E_\mu$, $\|f\|_E \leqslant \mu$ and $B^*(f)$ is the indicator function over E_1. Then the functional to minimize is

$$F_{\lambda,\mu}^{AC}(u, v) = J(u) + B^*\left(\frac{v}{\mu}\right) + (2\lambda)^{-1}\|f - u - v\|_{L^2}^2. \tag{68}$$

15

Figure 2: Original Barbara, House, and Leopard images.

Structures   Textures

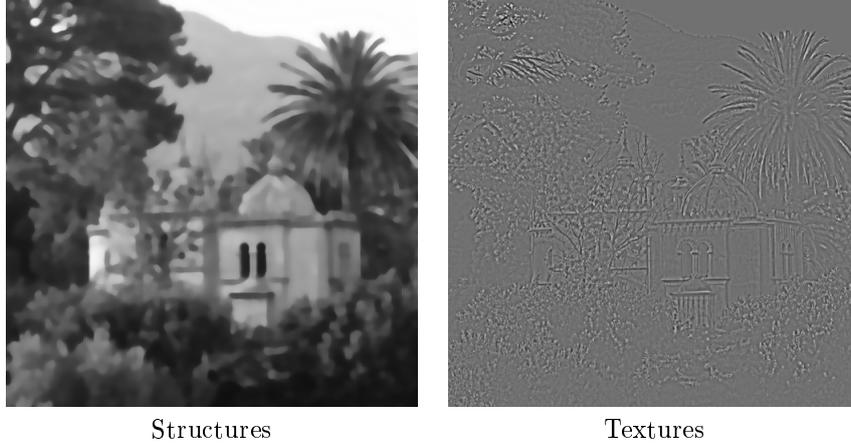Figure 3: BV-G structures + textures image decomposition of Barbara image.

Structures   Textures

Figure 4: BV-G structures + textures image decomposition of House image.

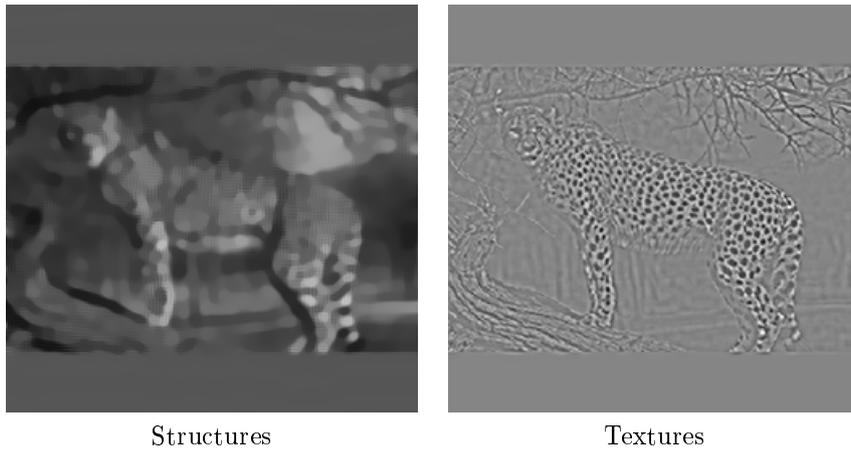Structures   Textures

Figure 5: BV-G structures + textures image decomposition of Leopard image.

Chambolle et al. (1998) proved the existence of a projector on this space, denoted P_{E_μ}, defined by

$$P_{E_\mu}(f) = f - WST(f, 2\mu), \tag{69}$$

where WST is the wavelet soft thresholding operator (we mean that we first perform the wavelet expansion of the function, then we do the soft thresholding of the wavelet coefficients, and end by reconstructing the image). Then the new numerical algorithm is as follows:

1. Initialization:
$$u_0 = v_0 = 0$$

17

2. Iteration $n + 1$:

$$v_{n+1} = P_{E_\mu}(f - u_n) = f - u_n - WST(f - u_n, 2\mu)$$
$$u_{n+1} = f - v_{n+1} - P_{G_\lambda}(f - v_{n+1})$$

3. We stop if

$$\max\left(|u_{n+1} - u_n|, |v_{n+1} - v_n|\right) \leqslant \epsilon$$

or if we reach a prescribed maximal number of iterations.

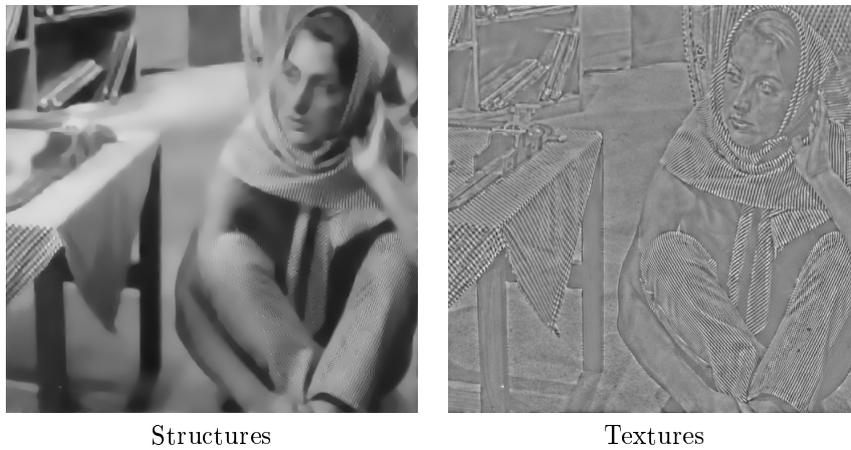The results obtained by this model are presented in Figures 6, 7, and 8.

Structures   Textures

Figure 6: BV-E_μ structures + textures image decomposition of Barbara image.
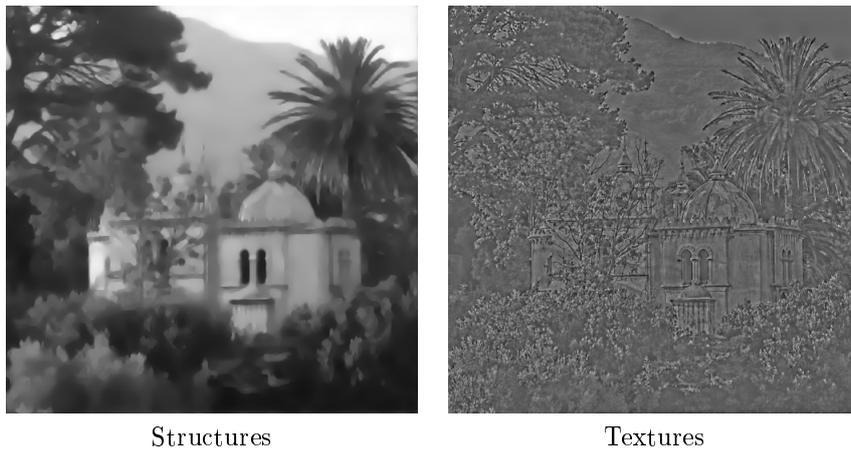

Structures   Textures

Figure 7: BV-E_μ structures + textures image decomposition of House image.

This algorithm works, but its main drawback is that it captures some structures informations (like the legs of the table in the Barbara image; see Figure 6). This behavior
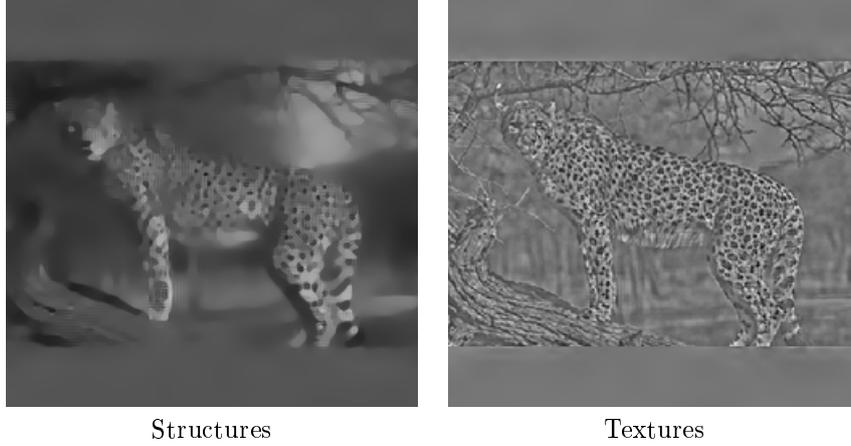
18

| Structures | Textures |

Figure 8: BV-E_μ structures + textures image decomposition of Leopard image.

appears because the space E is much bigger than the space G, in particular the space E contains functions that are not only textures.

Osher et al. (2002) explore the possibility of replacing the space G by the Sobolev space H^{-1}. They propose the following functional (v is obtained by $v = f - u$):

$$F_\lambda^{VS}(u) = J(u) + \lambda\|f - u\|_{H^{-1}}^2, \tag{70}$$

where $\|v\|_{H^{-1}} = \int |\nabla(\Delta^{-1})v|^2 dx dy$. The authors give the corresponding Euler-Lagrange equations and their discretization. Another way to numerically solve the problem is to use a modified version of Chambolle's projector $P_{H_\lambda^{-1}}$ (see Appendix A). Figures 9, 10, and 11 present the results obtained with this algorithm.
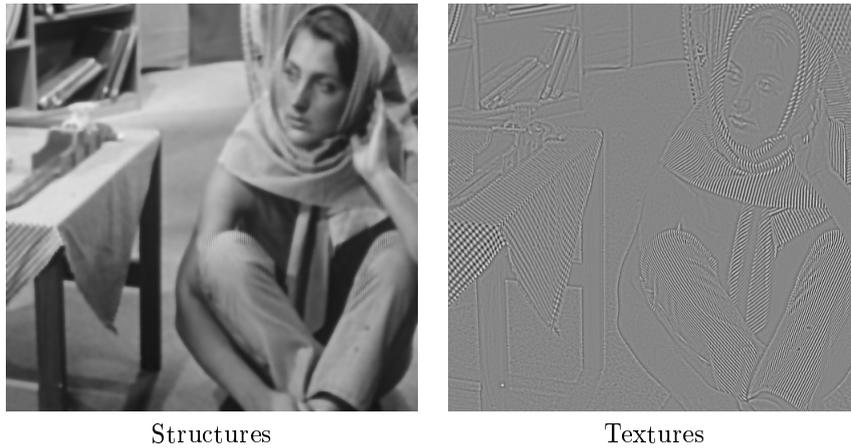

| Structures | Textures |

Figure 9: BV-H^{-1} structures + textures image decomposition of Barbara image.

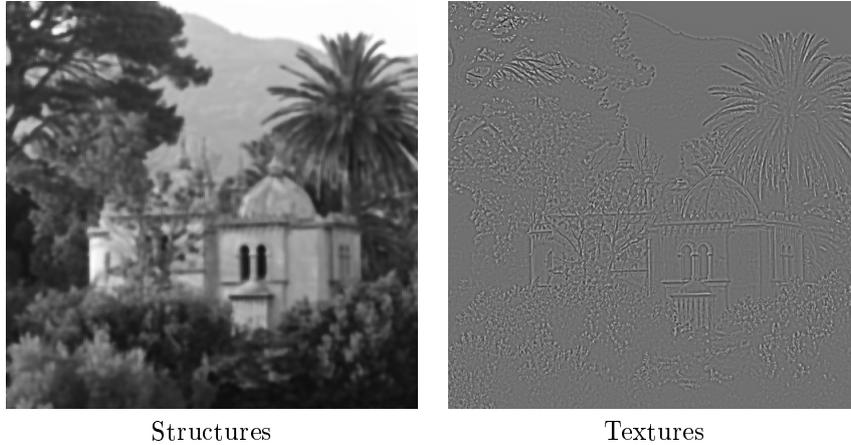Some other models were proposed that test different spaces to replace BV or G

19

Structures   Textures

Figure 10: BV-H^{-1} structures + textures image decomposition of House image.
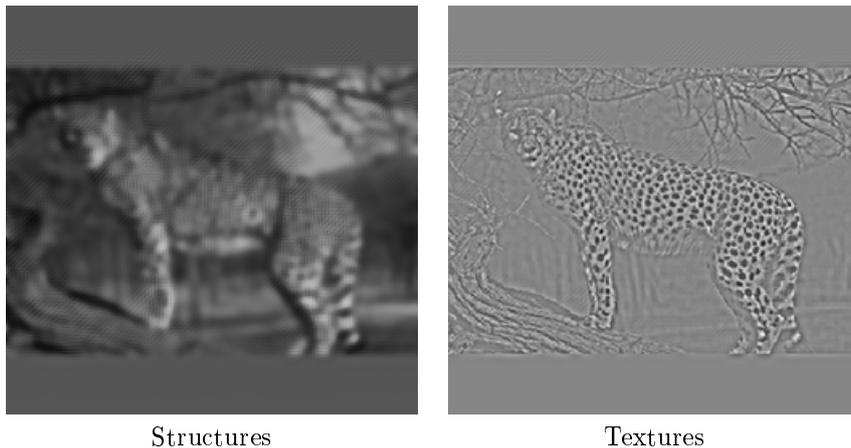

Structures   Textures

Figure 11: BV-H^{-1} structures + textures image decomposition of Leopard image.

spaces. We mention the work of Aujol and Chambolle (2005); Aujol and Gilboa (2006) who propose replacing the space BV by the smaller Besov space $B^1_{1,1}$, or replacing G by some Hilbert spaces, which permits the possibility of extracting textures with a certain directionality. Haddad (2005) proposes using the Besov space $\dot{B}^1_{1,\infty}$, instead of BV (the norms over these two spaces are equivalent) with the L^2 norm for the v part. J.B. Garnett and Vese (2005); Triet and Vese (2005) study the use of the spaces div (BMO), $B\dot{M}O^{-\alpha}$, and $\dot{W}^{-\alpha,p}$ to modelize the textures component.

4. Structures + Textures + Noise Decomposition

The previous algorithms yield good results but are of limited interest for noisy images (we add a gaussian noise with $\sigma = 20$ on each test image of Figure 2; the corresponding

20

noisy test images can be viewed in Figure 12). Indeed, noise can be viewed as a very highly oscillatory function (this means that noise can be view as living in the space G). Therefore, the algorithms incorporate the noise in the textures components. Then the textures are corrupted by noise (see Figure 13 for example).
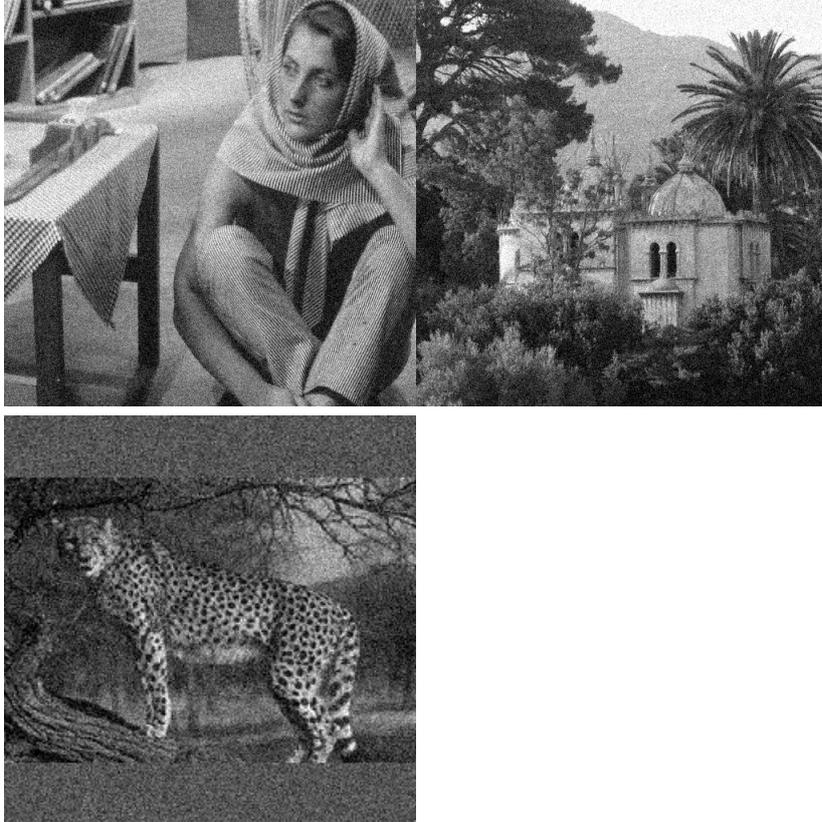

Figure 12: Original Barbara, House, and Leopard images corrupted by gaussian noise ($\sigma = 20$).

In this section, we present some extension of the two-component model to the three-component model, $f = u+v+w$, which could discriminate among structures (u), textures (v), and noise (w).

4.1. BV-G-G Local Adaptative Model

In Gilles (2007b), we proposed a new model to decompose an image into three parts: structures (u), textures (v), and noise (w). As in the $u + v$ model, we consider that structures and textures are modelized by functions in BV and G spaces, respectively. We also consider a zero mean gaussian noise added to the image. Let us view noise as a specific very oscillating function. In virtue of Meyer's work (Meyer (2001)), where it is shown that the more a function is oscillatory, the smaller its G-norm is, we propose
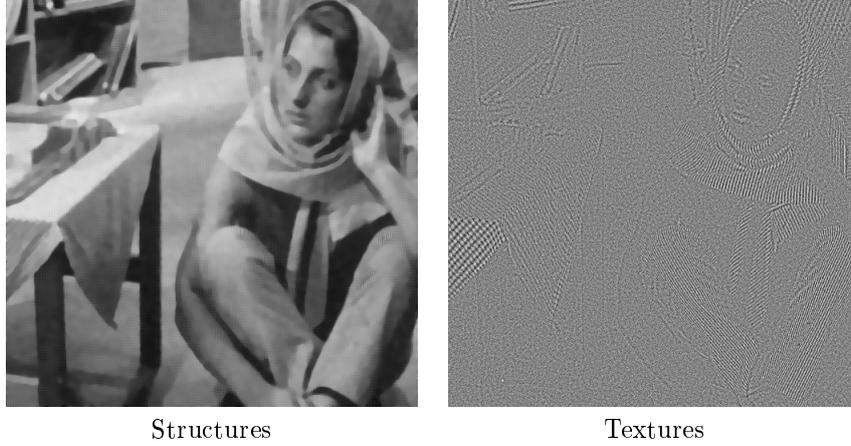
Structures   Textures

Figure 13: BV-G structures + textures image decomposition of the noisy Barbara image.

to modelize w as a function in G and consider that its G-norm is much smaller than the norm of textures ($\|v\|_G \gg \|w\|_G$). These assumptions are equivalent to choosing

$$v \in G_{\mu_1} \ , \ w \in G_{\mu_2}, \qquad \text{where} \quad \mu_1 \gg \mu_2. \tag{71}$$

To increase the performance, we propose adding a local adaptability behavior to the algorithm following an idea proposed by Gilboa et al. (2003). These authors investigate the ROF model given by Eq.(51) and propose a modified version that can preserve textures in the denoising process. To do this, they do not choose λ as a constant on the entire image but as a function $\lambda(f)(x,y)$ which represents local properties of the image. In a cartoon-type region, the algorithm enhances the denoising process by increasing the value of λ; in a texture-type region, the algorithm decreases λ to attenuate the regularization to preserve the details of textures. So $\lambda(f)(x,y)$ can be viewed as a smoothed partition between textured and untextured regions.

Then, in order to decompose an image into three parts, we propose to use the following functional:

$$F_{\lambda,\mu_1,\mu_2}^{JG}(u,v,w) = J(u) + J^*\left(\frac{v}{\mu_1}\right) + J^*\left(\frac{w}{\mu_2}\right) + (2\lambda)^{-1}\|f - u - \nu_1 v - \nu_2 w\|_{L^2}^2, \quad (72)$$

where the functions ν_i represent the smoothed partition of textured and untextured regions (and play the role of λ in Gilboa's paper). The ν_i functions must have the following behavior:

- for a textured region, we want to favor v instead of w. This is equivalent to ν_1 close to 1 and ν_2 close to 0,

- for an untextured region, we want to favor w instead of v. This is equivalent to ν_1 closed to 0 and ν_2 close to 1.

22

We see that ν_1 and ν_2 are complementary, so it is natural to choose $\nu_2 = 1 - \nu_1$: $\mathbb{R}^2 \to]0;1[$. The choice of ν_1 and ν_2 is discussed after the following proposition, which characterizes the minimizers of $F^{JG}_{\lambda,\mu_1,\mu_2}(u,v,w)$.

Proposition 3 *Let $u \in BV$, $v \in G_{\mu_1}$, and $w \in G_{\mu_2}$ be the structures, textures, and noise parts, respectively, and f the original noisy image. Let the functions $(\nu_1(f)(.,.), \nu_2(f)(.,.))$ be defined on $\mathbb{R}^2 \to]0;1[$, and assume that these functions could be considered as locally constant compared to the variation of v and w. Then a minimizer defined by*

$$(\hat{u}, \hat{v}, \hat{w}) = \underset{(u,v,w) \in BV \times G_{\mu_1} \times G_{\mu_2}}{\arg} \min F^{JG}_{\lambda,\mu_1,\mu_2}(u,v,w), \tag{73}$$

is given by

$$\hat{u} = f - \nu_1 \hat{v} - \nu_2 \hat{w} - P_{G_\lambda}(f - \nu_1 \hat{v} - \nu_2 \hat{w}), \tag{74}$$

$$\hat{v} = P_{G_{\mu_1}}\left(\frac{f - \hat{u} - \nu_2 \hat{w}}{\nu_1}\right), \tag{75}$$

$$\hat{w} = P_{G_{\mu_2}}\left(\frac{f - \hat{u} - \nu_1 \hat{v}}{\nu_2}\right), \tag{76}$$

where P_{G_μ} denotes Chambolle's non-linear projectors (see Appendix A).

The proof of this proposition can be found in Gilles (2007b). As in the two-part BV-G decomposition model, we get an equivalent numerical scheme:

1. Initialization: $u_0 = v_0 = w_0 = 0$,
2. Compute ν_1 and $\nu_2 = 1 - \nu_1$ from f,
3. Compute $w_{n+1} = P_{G_{\mu_2}}\left(\frac{f - u_n - \nu_1 v_n}{\nu_2 + \kappa}\right)$, ($\kappa$ is a small value in order to prevent the division by zero),
4. Compute $v_{n+1} = P_{G_{\mu_1}}\left(\frac{f - u_n - \nu_2 w_{n+1}}{\nu_1 + \kappa}\right)$,
5. Compute $u_{n+1} = f - \nu_1 v_{n+1} - \nu_2 w_{n+1} - P_{G_\lambda}(f - \nu_1 v_{n+1} - \nu_2 w_{n+1})$,
6. If $\max\{|u_{n+1} - u_n|, |v_{n+1} - v_n|, |w_{n+1} - w_n|\} \leqslant \epsilon$ or if we did N_{step} iterations then stop the algorithm, else jump to step 3.

Concerning the choice of the ν_i functions, we were inspired by the work of Gilboa et al. (2003). The authors choose to compute a local variance on the texture + noise part of the image obtained by the ROF model ($f - u$). In our model, we use the same strategy but on the v component obtained by the two parts decomposition algorithm. This choice is implied by the fact that the additive gaussian noise can be considered as orthogonal to textures. As a consequence, the variance of a textured region is larger than the variance of an untextured region.

So, in practice, we first compute the two-part decomposition of the image f. On the textures part, for all the pixels (i, j), we compute the local variance on a small window (odd size L) centered on (i, j). At the least, we normalized it to obtain the values in $]0;1[$. All the details about the computation of the ν_i's function can be found in Gilles

Figure 14: Texture partition ν_1 obtained by local variance computation.
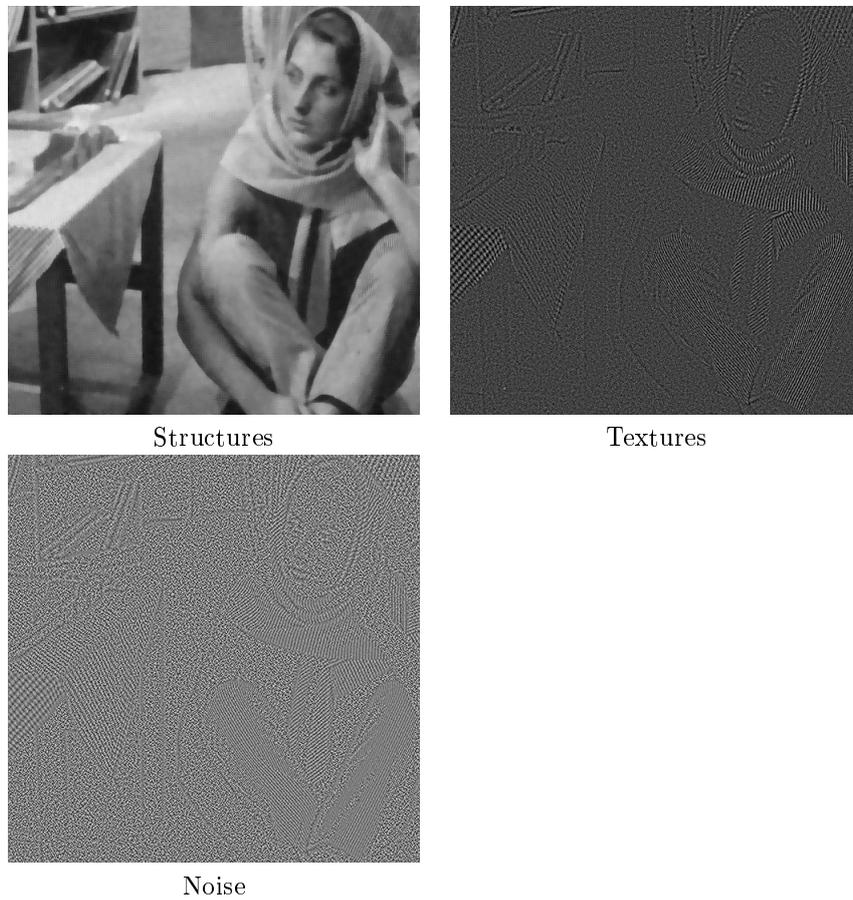

Structures

Textures

Noise

Figure 15: *BV-G-G* structures + textures + noise image decomposition of Barbara image.

(2007b). Figure 14 shows an example from the noisy Barbara image. As expected, the variance is higher in the textured regions and lower in the others.

Structures

Textures

Noise

Figure 16: *BV-G-G* structures + textures + noise image decomposition of House image.

Figures 15, 16, and 17 show the results of the $u + v + w$ decomposition we obtained by the *BV-G-G* local adaptive model. This model can separate noise from the textures. If we look more precisely, we can see that some residual noise remains in the textures, and some textures are partially captured in the noise part. This is due to the choice of the parameters λ, μ_1, and μ_2 which act on the separability power of the algorithm.

4.2. Aujol-Chambolle BV-G-E Model

The same time as our work, Aujol and Chambolle (2005) thought of the same structures + textures + noise decomposition problem. They proposed a model close to our model described in the previous subsection but with the difference that they consider the noise as a distribution taken in the Besov space $E = \dot{B}^{\infty}_{-1,\infty}$. Then the associated functional is

$$F^{AC2}_{\lambda,\mu,\delta}(u,v,w) = J(u) + J^* \left(\frac{v}{\mu} \right) + B^* \left(\frac{w}{\delta} \right) + (2\lambda)^{-1} \| f - u - v - w \|^2_{L^2}, \qquad (77)$$

25

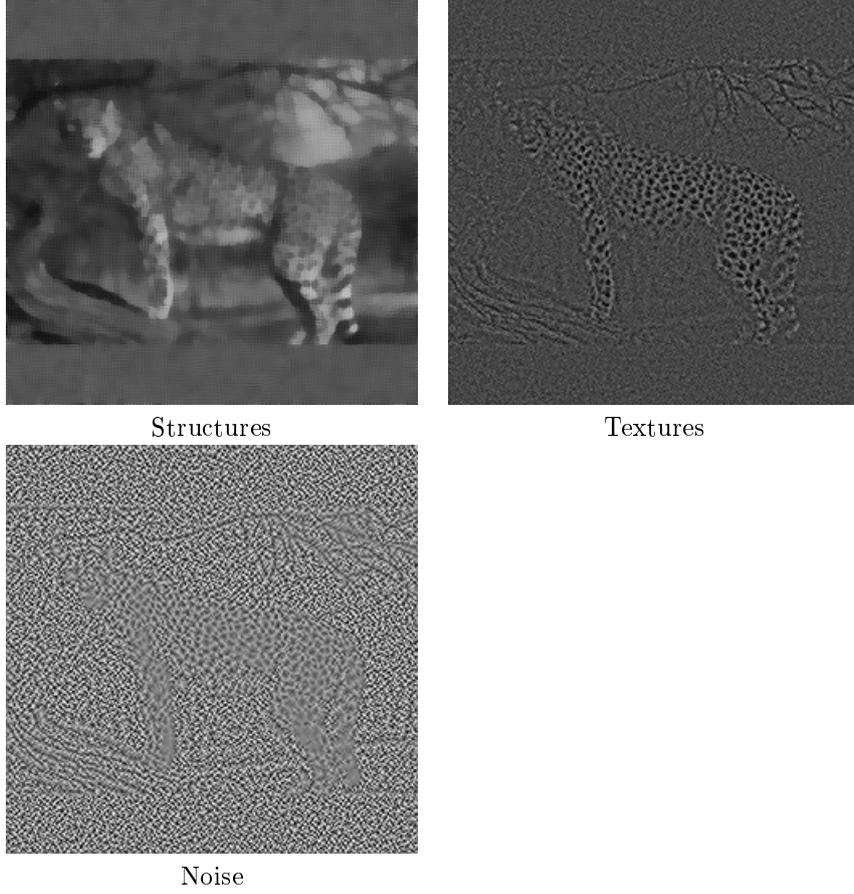<center>Structures   Textures</center>

<center>Noise</center>

Figure 17: *BV-G-G* structures + textures + noise image decomposition of Leopard image.

where $u \in BV$, $v \in G_\mu$, and $w \in E_\delta$ as defined in the previous sections. The authors prove that the minimizers are (see Aujol and Chambolle (2005)):

$$\hat{u} = f - \hat{v} - \hat{w} - P_{G_\lambda}(f - \hat{v} - \hat{w}), \qquad (78)$$

$$\hat{v} = P_{G_\mu}(f - \hat{u} - \hat{w}), \qquad (79)$$

$$\hat{w} = P_{E_\delta}(f - \hat{u} - \hat{v}) = f - \hat{u} - \hat{v} - WST(f - \hat{u} - \hat{v}, 2\delta), \qquad (80)$$

where $WST(f - \hat{u} - \hat{v}, 2\delta)$ is the Wavelet Soft Thresholding operator applied on $f - \hat{u} - \hat{v}$ with a threshold set to 2δ.

Then the numerical algorithm is given by

1. Initialization: $u_0 = v_0 = w_0 = 0$,
2. Compute $w_{n+1} = f - u_n - v_n - WST(f - u_n - v_n, 2\delta)$,
3. Compute $v_{n+1} = P_{G_\mu}(f - u_n - w_{n+1})$,
4. Compute $u_{n+1} = f - v_{n+1} - w_{n+1} - P_{G_\lambda}(f - v_{n+1} - w_{n+1})$,

<center>26</center>

5. If $\max\{|u_{n+1} - u_n|, |v_{n+1} - v_n|, |w_{n+1} - w_n|\} \leqslant \epsilon$ or if we performed N_{step} iterations, then stop the algorithm, else jump to step 2.

The results of this algorithm on our test images are shown in Figures 18, 19, and 20, respectively. We can see that textures are better denoised by this model. This is a consequence of a better noise modeling by distributions in the Besov space. But the residual texture is more important than the one given by our algorithm in the noise part. Another drawback appears in the structures part; the edges in the image are damaged because some important wavelet coefficients are removed. Previously, Gilles (2007b) provides the possibility to add the local adaptivity behavior of the *BV-G-G* model to the *BV-G-E* model. We refer the reader to Gilles (2007b) to see the *BV-G-E* local adaptivity functional and find the corresponding results. This modified version shows less improvement compared to the original. We prefer to explore the replacement of wavelets by new geometric multiresolution tools such as contourlets.
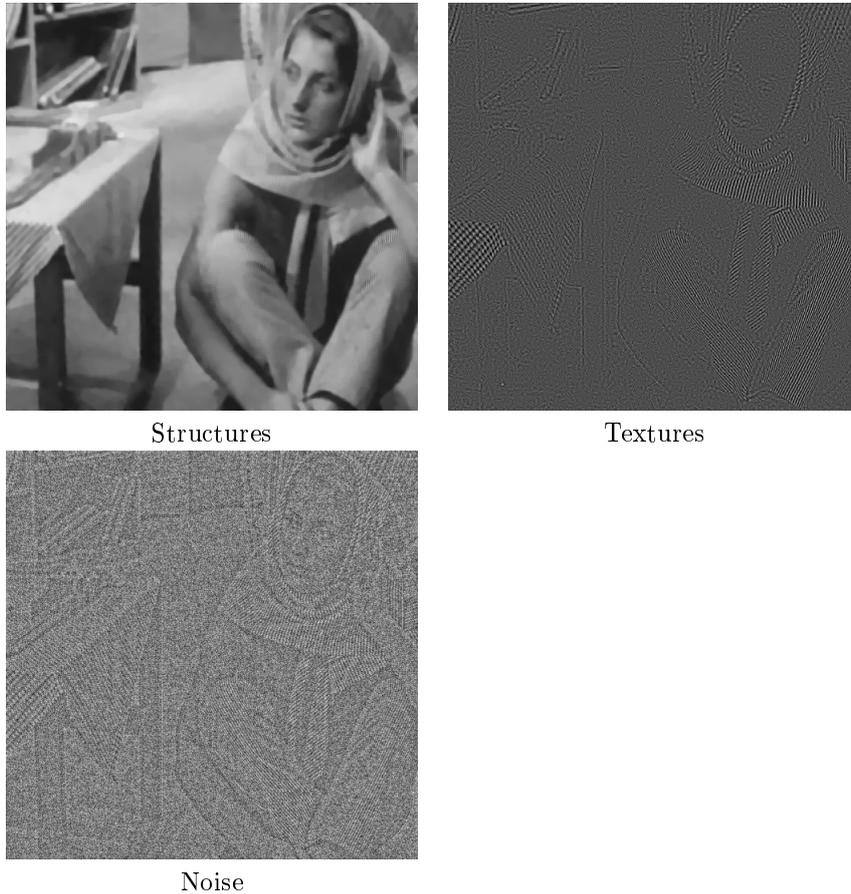

Structures   Textures

Noise

Figure 18: *BV-G-E* structures + textures + noise image decomposition of Barbara image.
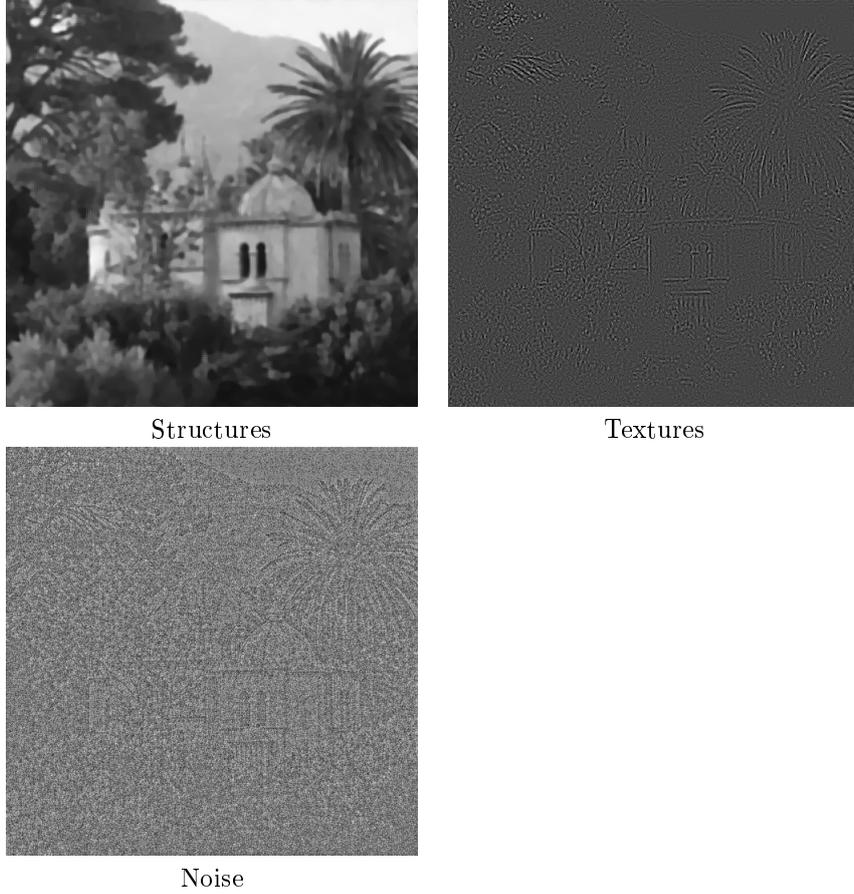
27

Structures

Textures

Noise

Figure 19: *BV-G-E* structures + textures + noise image decomposition of House image.

4.3. The BV-G-$\dot{C}o^{\infty}_{-1,\infty}$ Decomposition Model

As mentionned previously, the new directional multiresolution tools, such as curvelets or contourlets, exhibit very good results in denoising. They also better reconstruct the edge in an image. So, the idea to replace the use of wavelet by curvelets or contourlets naturally arises. In this paper, we focus on the choice of contourlets. This choice is equivalent to changing the Besov space in the model described in the previous subsection by the homogeneous contourlet space $\dot{C}o^{\infty}_{-1,\infty}$. Then, the equivalent functional is given in Eq.(81) as below:

$$F^{Co}_{\lambda,\mu,\delta}(u,v,w) = J(u) + J^{*}\left(\frac{v}{\mu}\right) + J^{*}_{Co}\left(\frac{w}{\delta}\right) + (2\lambda)^{-1}\|f-u-v-w\|^{2}_{L^{2}}, \qquad (81)$$

28

<div align="center">Structures   Textures</div>

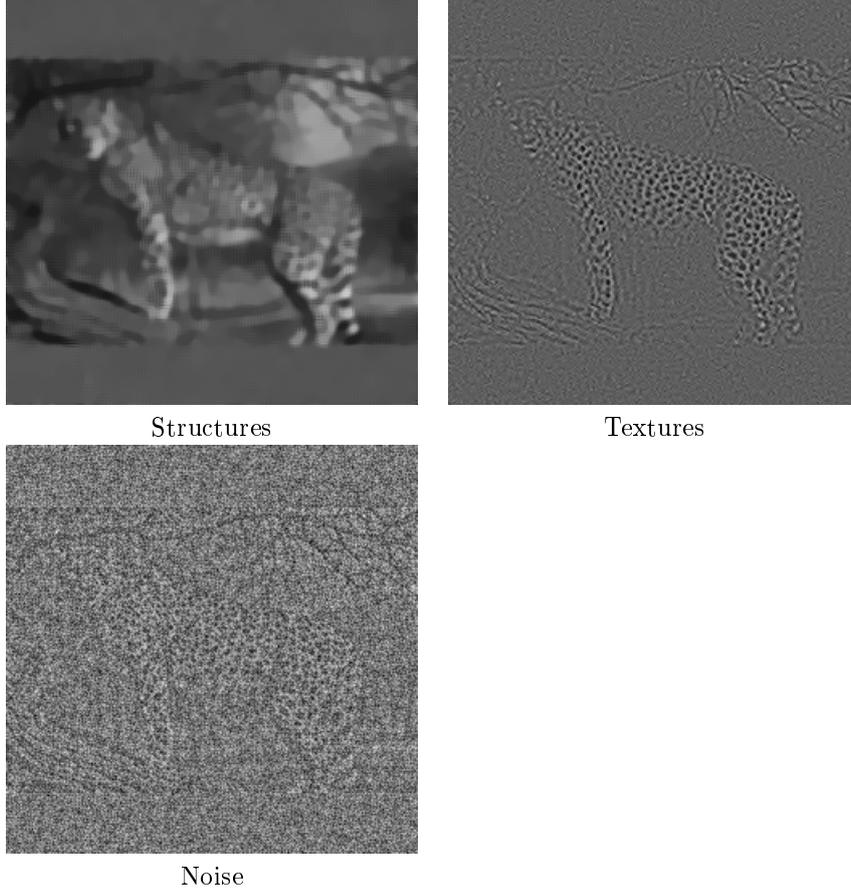<div align="center">Noise</div>

<div align="center">Figure 20: <i>BV-G-E</i> structures + textures + noise image decomposition of Leopard image.</div>

where $J_{Co}^*(f)$ is the indicator function over the set Co_1 if we denote $Co_\delta = \left\{ f \in Co_{-1,\infty}^\infty / \|f\|_{Co_{-1,\infty}^\infty} \leqslant \delta \right\}$ (norm over the contourlet spaces is defined in the subsection 2.7.4) defined by

$$J_{Co}^*(f) = \begin{cases} 0 & \text{if } f \in Co_1 \\ +\infty & \text{else.} \end{cases} \tag{82}$$

Then, the following proposition gives the solutions that minimize the previous functional.

Proposition 4 *Let $u \in BV$, $v \in G_\mu$, $w \in Co_\delta$ be the structures, textures, and noise components derived from the image decomposition. Then the solution*

$$(\hat{u}, \hat{v}, \hat{w}) = \underset{(u,v,w) \in BV \times G_\mu \times Co_\delta}{\arg} \inf F_{\lambda,\mu,\delta}^{Co}(u, v, w) \tag{83}$$

<div align="center">29</div>

is given by

$$\hat{u} = f - \hat{v} - \hat{w} - P_{G_\lambda}(f - \hat{v} - \hat{w})$$
$$\hat{v} = P_{G_\mu}(f - \hat{u} - \hat{w})$$
$$\hat{w} = f - \hat{u} - \hat{v} - CST(f - \hat{u} - \hat{v}; 2\delta),$$

where P_{G_λ} is the Chambolle nonlinear projector and $CST(f, 2\delta)$ is the contourlet soft thresholding operator of $f - u - v$.

PROOF. The components $\hat{u}, \hat{v}$ are obtained by the same arguments used in the proof of Proposition 3 (this proof is available in Gilles (2007b)). The particular point concerns the expression of $\hat{w}$ expressed with the soft thresholding of the contourlet coefficients. Assume we want to minimize $F_{\lambda,\mu,\delta}^{Co}(u, v, w)$ compared to w; it is equivalent to find w solution of (we set $g = f - u - v$)

$$\hat{w} = \arg_{w \in Co_\delta} \min \left\{ \|g - w\|_{L^2}^2 \right\}. \tag{84}$$

We can replace it by its dual formulation: $\hat{w} = g - \hat{h}$, such that

$$\hat{h} = \arg_{h \in Co_{1,1}^1} \min \left\{ 2\delta \|h\|_{Co_{1,1}^1} + \|g - h\|_{L^2}^2 \right\}. \tag{85}$$

We can use the same approach used by Chambolle et al. (1998).

Let $(c_{j,k,n})_{j \in \mathbb{Z}, 0 \leqslant k \leqslant 2^{(l_j)}, n \in \mathbb{Z}^2}$ and $(d_{j,k,n})_{j \in \mathbb{Z}, 0 \leqslant k \leqslant 2^{(l_j)}, n \in \mathbb{Z}^2}$ denote the coefficients issued from the contourlet expansions of g and h, respectively. As contourlets form a tight frame, with a bound of 1, we have (we denote $\Omega = \mathbb{Z} \times [\![0, 2^{(l_j)}]\!] \times \mathbb{Z}^2$)

$$\|g\|_{L_2}^2 = \sum_{(j,k,n) \in \Omega} |c_{j,k,n}|^2. \tag{86}$$

Then Eq.(85) can be rewritten as

$$\sum_{(j,k,n) \in \Omega} |c_{j,k,n} - d_{j,k,n}|^2 + 2\delta \sum_{(j,k,n) \in \Omega} |d_{j,k,n}|, \tag{87}$$

which is equivalent to

$$|c_{j,k,n} - d_{j,k,n}|^2 + 2\delta |d_{j,k,n}|. \tag{88}$$

However, Chambolle et al. (1998) prove that the solution of this kind of problem is the soft thresholding of the coefficients $(c_{j,k,n})$ with 2δ as the threshold.

Then $\hat{h} = CST(g, 2\delta)$, which by duality implies that $\hat{w} = g - CST(g, 2\delta)$. We conclude that

$$\hat{w} = f - \hat{u} - \hat{v} - CST(f - \hat{u} - \hat{v}, 2\delta) \tag{89}$$

which end the proof.

The corresponding numerical scheme is the same as in the *BV-G-E* algorithm, except we replace the wavelet expansion by the contourlet expansion in the soft thresholding:

1. Initialization: $u_0 = v_0 = w_0 = 0$,
2. Compute $w_{n+1} = f - u_n - v_n - CST(f - u_n - v_n, 2\delta)$,
3. Compute $v_{n+1} = P_{G_\mu}(f - u_n - w_{n+1})$,
4. Compute $u_{n+1} = f - v_{n+1} - w_{n+1} - P_{G_\lambda}(f - v_{n+1} - w_{n+1})$,
5. If $\max\{|u_{n+1} - u_n|, |v_{n+1} - v_n|, |w_{n+1} - w_n|\} \leqslant \epsilon$ or if we performed N_{step} iterations, then stop the algorithm; else jump to step 2.

Figures 21, 22, and 23 show the results obtained by replacing wavelets by contourlets. The advantage of using geometric frames is that it preserves well the integrity of oriented textures as seen in the zoomed images in Figure 24.

In this section, we presented many decomposition models. We can imagine the use of other frames and basis like curvelets, cosines, and so on. The idea of decomposing an image by thresholding different basis expansion coefficients corresponds to the recent theory of morphological component analysis (MCA) (J. Bobin and Moudden (2007); J. Bobin and Donoho (2007)). This approach seeks sparse representation of the different components and is useful for sources separation.

5. Performance Evaluation

The previous section described different decomposition models based on specific function spaces. But one question arises: Which is the best one?

This section adresses this question by defining well-adapted criteria and their associated metrics. We build a special test image by creating different components separately and then by adding them. We will denote f_0 the test image composed of u_0 (the structures reference image) + v_0 (the textures reference image) + w_0 (the noise reference image). We finish by giving the measures obtained for this image.

5.1. Test Image

Because we want to compare the quality of each extracted components, we will create specific components: u_0 for structures, v_0 for textures, and w_0 for noise. Textures are built by sine functions over some finite domains; structures are made by drawing some shapes with an adapted software like GIMP. The noise part is simply a gaussian noise with $\sigma = 20$. The u_0 and v_0 reference parts and the recomposed test image are shown in Figure 25.

5.2. Evaluation Metrics

Assume the test image is composed of known reference images u_0, v_0, and w_0. We choose the following criteria to measure the decomposition quality: the L^2-norms of errors $u - u_0$ and $v - v_0$, where u and v are the structures and textures components issued from the decomposition. Another quantity that is interesting to evaluate is the residual structures + textures present in the noise component w. To measure this quantity we prove the following proposition.
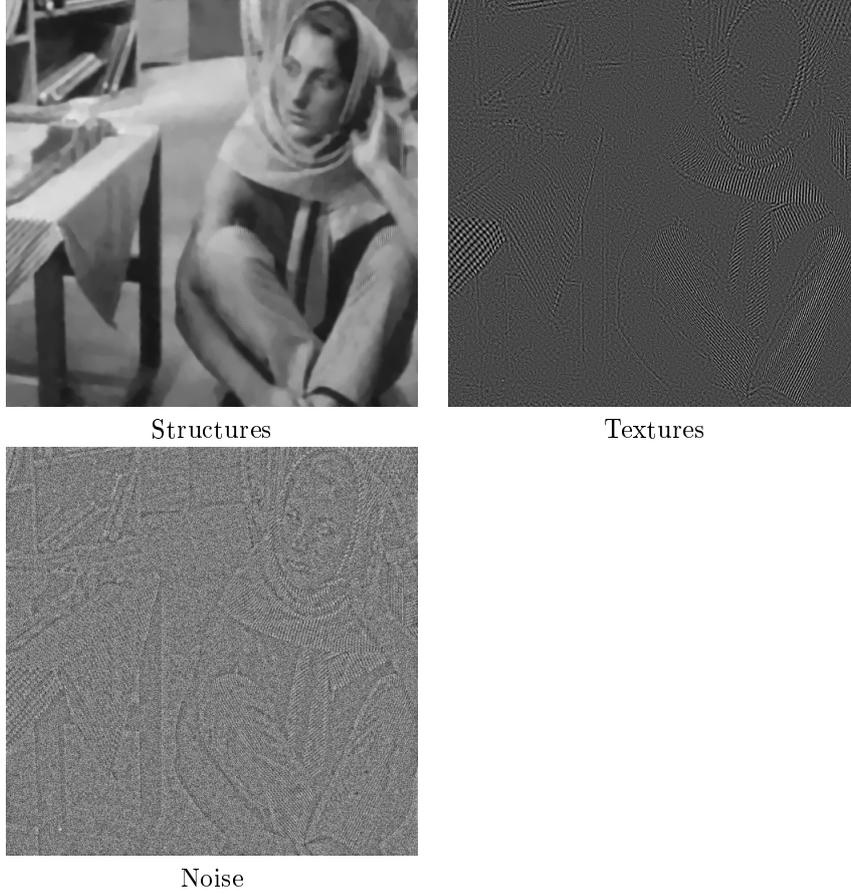
Structures

Textures

Noise

Figure 21: *BV-G-Co* structures + textures + noise image decomposition of Barbara image.

Proposition 5 *Let $b(i,j)$ denote a gaussian noise of variance σ^2 and $d(i,j)$ an image free of noise (we assume that the intercorrelation between b and d is negligible). Let $f = Ad + b$ be a simulated noise + residue image where $A \in \mathbb{R}$ corresponds to residue level. Then*

$$\|\gamma_f - \gamma_b\|_{L^2} \approx A^2, \tag{90}$$

where γ_f and γ_b are the autocorrelation functions of f and b, respectively.

PROOF. We start by calculating the autocorrelation function of f:

$$\gamma_f(k,l) = \sum_{(i,j) \in \mathbb{Z}^2} f(i,j)f^*(i+k,j+l). \tag{91}$$

32

<div align="center">Structures   Textures</div>
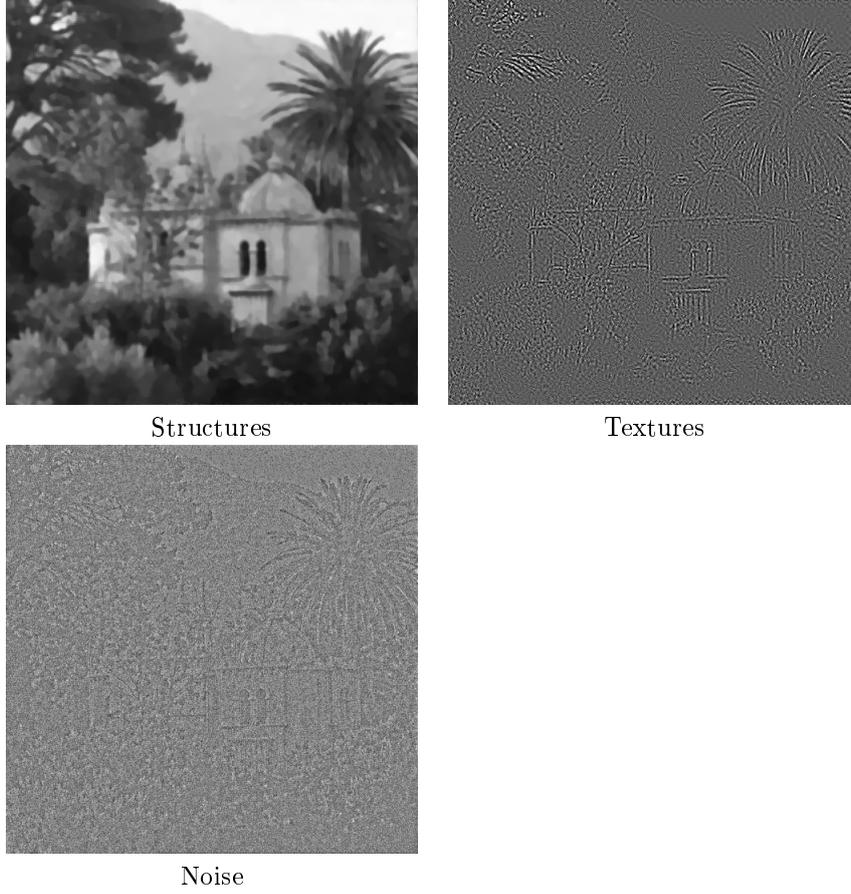
<div align="center">Noise</div>

Figure 22: *BV-G-Co* structures + textures + noise image decomposition of House image.

However, we assume that images are real, then $f(i,j) = f^*(i,j)$ and we deduce that

$$\gamma_f(k,l) = \sum_{(i,j)\in\mathbb{Z}^2} [Ad(i,j) + b(i,j)][Ad(i+k,j+l) + b(i+k,j+l)] \tag{92}$$

$$= \sum_{(i,j)\in\mathbb{Z}^2} A^2 d(i,j)d(i+k,j+l) + \sum_{(i,j)\in\mathbb{Z}^2} b(i,j)b(i+k,j+k) +$$

$$\sum_{(i,j)\in\mathbb{Z}^2} [Ad(i,j)b(i+k,j+l) + Ad(i+k,j+l)b(i,j)] \tag{93}$$

$$= A^2\gamma_d(k,l) + \gamma_b(k,l) + A(\gamma_{db}(k,l) + \gamma_{bd}(k,l)) \tag{94}$$

Now we examine the norm $\|.\|_{L^2}$ of this autocorrelation function. First, notice that $\gamma_b(k,l) = \sigma^2 \delta(k,l)$ (where $\delta(k,l)$ is the Kronecker symbol) because we assumed that the noise is gaussian. The statement of the proposition assumed that the intercorrelations are negligible; in pratice, it is easy to check that the quantity $A(\gamma_{db}(k,l) + \gamma_{bd}(k,l))$ is

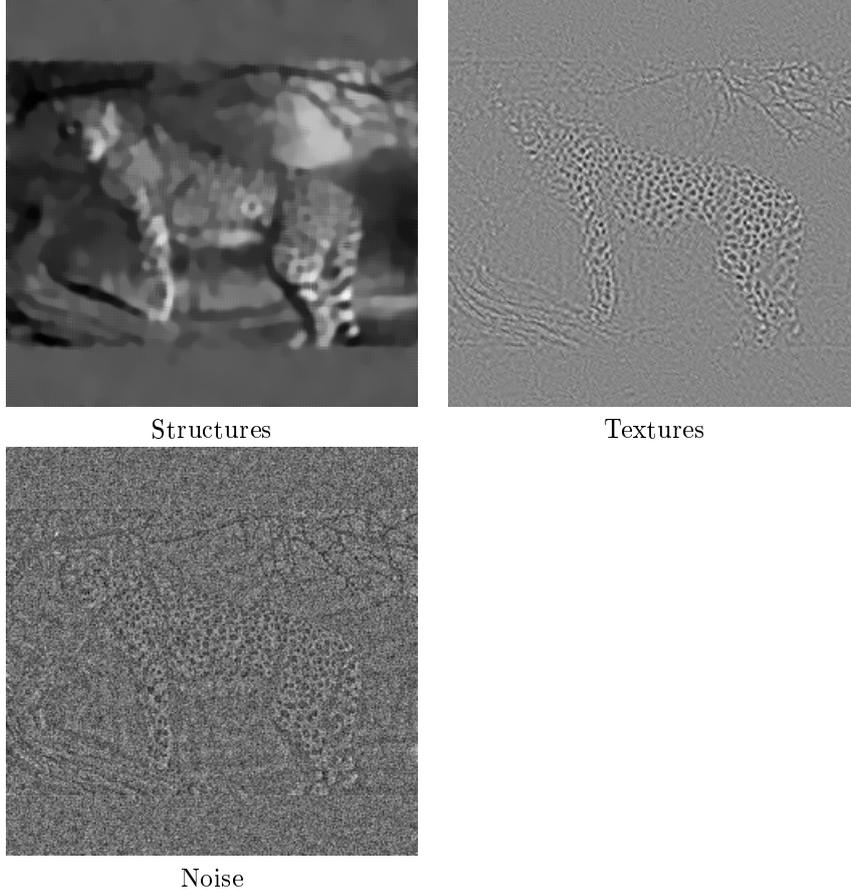<div align="center">33</div>

Structures

Textures

Noise

Figure 23: *BV-G-Co* structures + textures + noise image decomposition of Leopard image.

negligible compared to $A^2\gamma_d(k,l)$. We deduce that

$$\gamma_f(k,l) - \gamma_b(k,l) \approx A^2\gamma_d(k,l); \tag{95}$$

then, by passing to the norm, we get

$$\|\gamma_f - \gamma_b\|_{L^2} \approx A^2\|\gamma_d\|_{L^2}. \tag{96}$$

To illustrate this proposition, assume that we take the image in Figure 26 as $d(i,j)$ and we generate an image $b(i,j)$ full of gaussian noise ($\sigma = 20$). Then we compose the image $f = Ad + b$ for the different values $A \in \{0.05; 0.1; 0.2; 0.3; 0.4; 0.5; 0.6; 0.7; 0.8; 0.9\}$ (this means that more and more residue appears as A increases, see Figure 27 top row).

Figure 28 gives the measured values of $\|\gamma_f - \gamma_b\|_{L^2}$ and shows the associated graph. As announced by the proposition, we show the quadratic behavior of the norm of the autocorrelation differences as A grows. We will use this metric in the next subsection to evaluate the residual quantity in the noise parts at the output of the different decomposition algorithms.

Wavelet thresholding   Contourlet thresholding
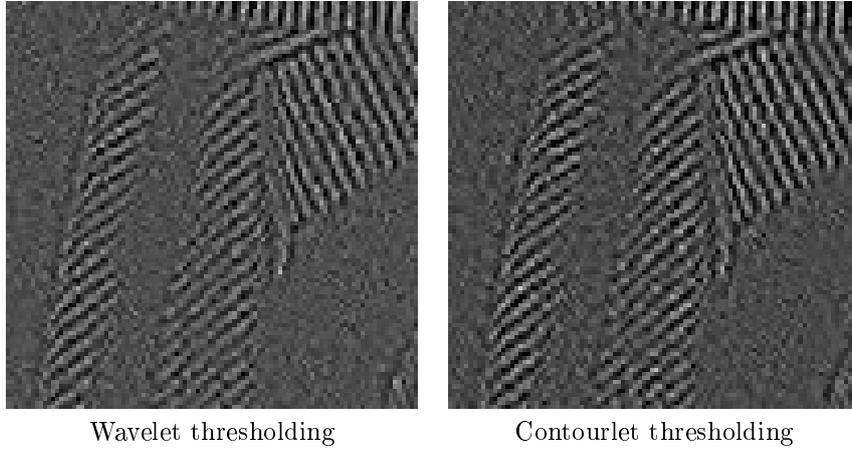
Figure 24: Zoomed image for the textured components of wavelet, and contourlet, based algorithms.
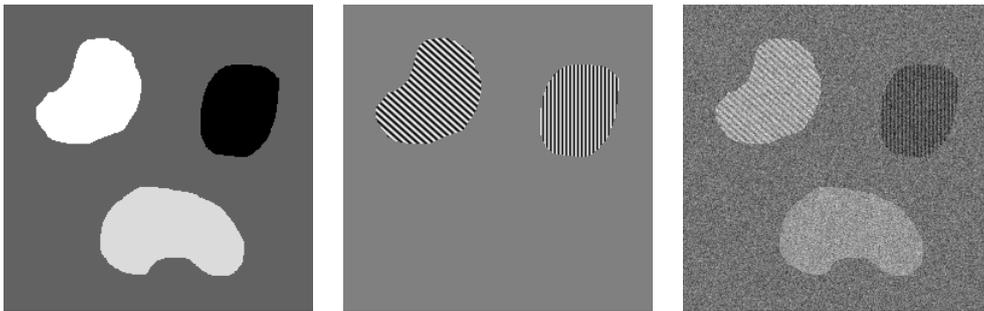

Figure 25: Structures and textures reference images and the recomposed test image.

Figure 26: Residual reference image.

5.3. Image Decomposition Performance Evaluation

In this subsection we apply three-part image decomposition on the test image built in subsection 5.1 and use the metrics defined in subsection 5.2 to evaluate their perfor-
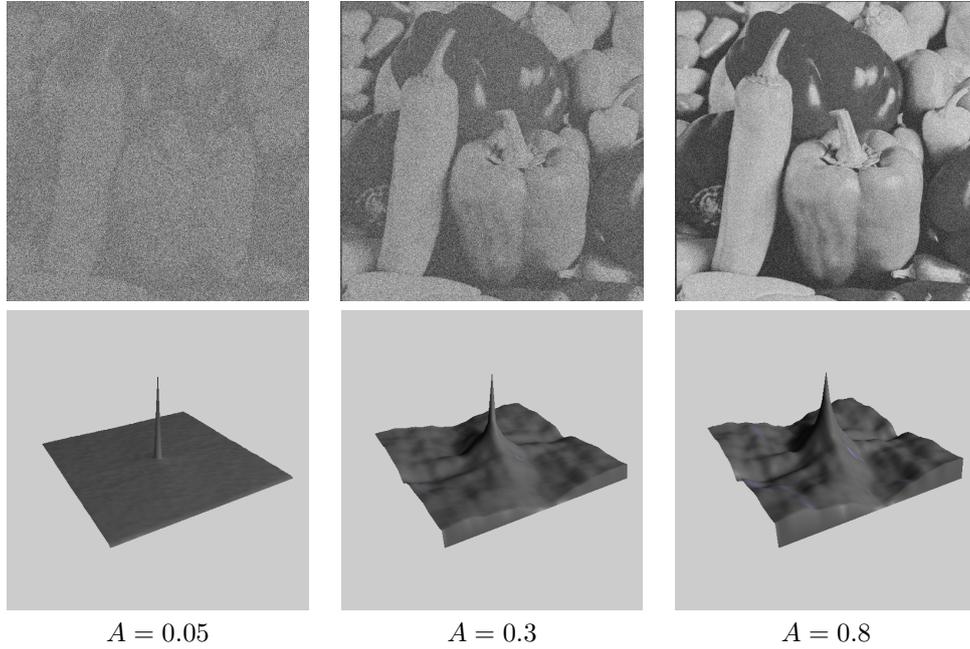
$$A = 0.05 \qquad A = 0.3 \qquad A = 0.8$$

Figure 27: Noisy reference images affected by different residual levels and their associated autocorrelation images.

A	$\|\gamma_f - \gamma_b\|_{L^2}$
0.05	849.093432
0.1	3312.071022
0.2	13099.095280
0.3	29367.800483
0.4	52118.223554
0.5	81350.371724
0.6	117064.247377
0.7	159259.851531
0.8	207937.184693
0.9	263096.247142
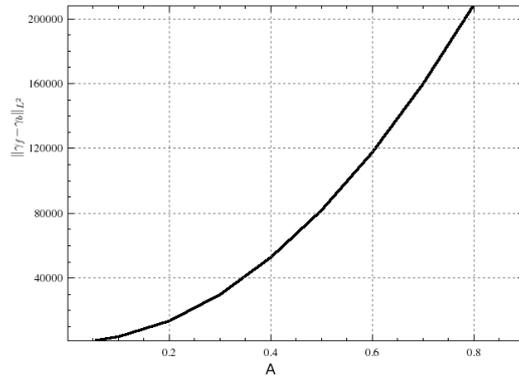
Figure 28: Results of the measure norm $\|\gamma_f - \gamma_b\|_{L^2}$ for the different values of A (left) and its associated graph.

mances. In this chapter, we restrict the choice of the different parameters to only the ones that give the best visual performances, but in the future, a more global, in terms of parameters variability, test could be to explore the complete behaviors of the algorithms. The choosen parameters are

- Algorithm F^{JG}: $\lambda = 10$, $\mu_1 = 1000$, $\mu_2 = 100$, and a window size of 3×3 pixels,

- Algorithm F^{AC2}: $\lambda = 1$, $\mu = 500$ and $\delta = 9.4$ ($\kappa = 0.2$ and $\sigma = 20$),

- Algorithm F^{Co}: $\lambda = 1$, $\mu = 500$ and $\delta = 23.5$ ($\kappa = 0.5$ and $\sigma = 20$).

Figure 29 shows the outputs of the different algorithms while table 1 gives the corresponding measures.
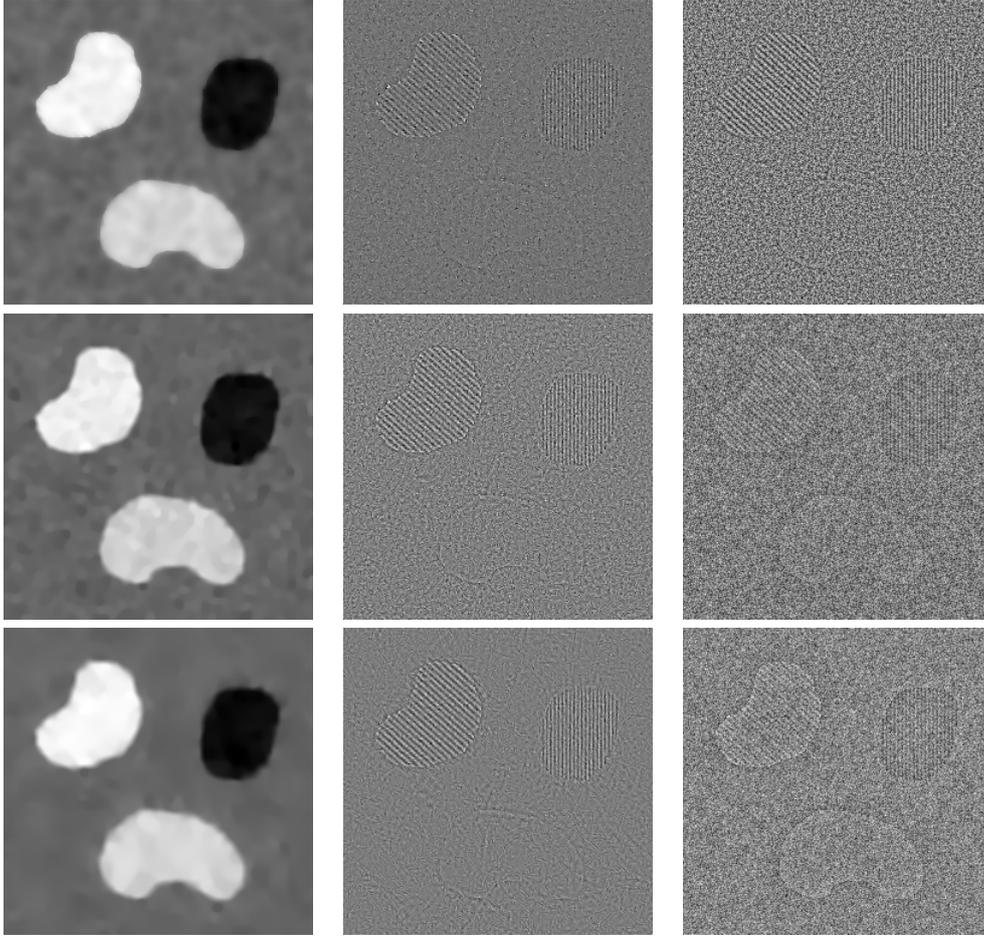
Figure 29: Outputs of the decomposition algorithms. First row: F^{JG} algorithm; second row: F^{AC2} algorithm; last row: F^{Co} algorithm.

We can see the BV-G-G-based algorithm F^{JG} has the smallest error for the structures image but the textures are slightly less preserved than the contourlet-based model F^{Co}. Its noisy part is of the same quality as the wavelet-based model F^{AC2}. Moreover, it is clear the F^{Co} algorithm gives the best denoising performance and has the least residue; it also has the best score for the textures quality. Even if the visual quality seems to be close to the F^{JG} algorithm, the contourlet-based model has the worst score on the structures

Algorithm	F^{JG}	F^{AC2}	F^{Co}
$\|\tilde{u} - u_0\|_{L^2}$	792.8	873.5	984.6
$\|\tilde{v} - v_0\|_{L^2}$	1844.9	2832.4	1598.6
$\|\gamma_w - \gamma_{w_0}\|_{L^2}$	423.2	423.5	255.3

Table 1: Evaluation Measures Obtained for All u, v, w Decomposition Algorithms.

component. Then globally, as expected, the model based on contourlet expansion gives the best decomposition.

6. Conclusion

This chapter provides an overview of structures + textures image decomposition. We also present the extension to noisy images decomposition and show that it is necessary to adopt a three-part decomposition model (structures + textures + noise). The different models are based on the bounded-variation space to describe the structures component of an image. The textures are defined by the space G of oscillating functions proposed by Meyer; different stategies can be used for the noise. Some other function spaces can be chosen; most often it is equivalent to choosing the best basis or frame to represent the different components. This approach is the same philosophy as the principle of morphological component analysis recently introduced by the work of J. Bobin and Moudden (2007); J. Bobin and Donoho (2007).

An interesting property used in the BV-G-G model is the local adaptibility of the algorithm by choosing a nonconstant parameter ν. Some recent theoretical work on the Besov and Triebel-Lizorkin spaces seems to provide some insight on the local behavior of an image (in terms of local scales). Here this approach is used to improve the quality of the decomposition.

The main problem of the decomposition models, and it remains an open question, is the choice of the different parameters. Aujol et al. (2006) propose a method of automatically selecting the parameter λ, but it is very expansive in computing time. We currently start some work to find some solutions.

We have proposed a method, which consists of building specific test images and using three different metrics, to evaluate the performance of the quality of components issued from the different decomposition algorithms. The first tests seem to confirm that the model based on the thresholding of contourlets coefficients is the best one. However, more complete tests based on different test images with different kind of textures, noise, or structures and by tuning the different parameters are needed. This could help us to understand completely the behaviors of this kind of algorithm.

The last topic explored in this study is the application of the image decomposition. A previous study, Gilles (2007a), proves that the BV-G model enhanced the thin and long structures. Then, we use the textures component as the input of a road detection algorithm in aerial images. We believe that many applications could be created in the future.

A. Chambolle's Nonlinear Projectors

Chambolle (2004) proposes an algorithm based on a nonlinear projector to solved a certain category of total variation based functional. This appendix summarizes this work. Some proofs are provided because they are relevant to the rest of the chapter.

A.1. Notations and Definitions

We assume the processed image is size $M \times N$. We denote $X = \mathbb{R}^{M \times N}$ and $Y = X \times X$.

Definition 6. Let $u \in X$; then the discret gradient of u, written $\nabla u \in Y = X \times X$, is defined by

$$(\nabla u)_{i,j} = \left((\nabla u)^1_{i,j}, (\nabla u)^2_{i,j} \right) \tag{97}$$

with $\forall i,j \in [\![0, \dots, M-1]\!] \times [\![0, \dots, N-1]\!]$

$$(\nabla u)^1_{i,j} = \begin{cases} u_{i+1,j} - u_{i,j} & \text{if} \quad i < M-1 \\ 0 & \text{if} \quad i = M-1 \end{cases} \tag{98}$$

$$(\nabla u)^2_{i,j} = \begin{cases} u_{i,j+1} - u_{i,j} & \text{if} \quad j < N-1 \\ 0 & \text{if} \quad j = N-1 \end{cases}. \tag{99}$$

Definition 7. Let $p \in Y$ ($p = (p^1, p^2)$), we define the numerical divergence operator $\text{div} : Y \to X$ such that $\text{div} = -\nabla^*$ (∇^* is the adjoint operator of ∇) by the following:

$$(\text{div } p)_{i,j} = \begin{cases} p^1_{i,j} - p^1_{i-1,j} & \text{if} \quad 0 < i < M-1 \\ p^1_{i,j} & \text{if} \quad i = 0 \\ -p^1_{i-1,j} & \text{if} \quad i = M-1 \end{cases} + \begin{cases} p^2_{i,j} - p^2_{i,j-1} & \text{if} \quad 0 < j < N-1 \\ p^2_{i,j} & \text{if} \quad j = 0 \\ -p^2_{i,j-1} & \text{if} \quad j = N-1 \end{cases}. \tag{100}$$

We recall that $\langle -\text{div } p, u \rangle_X = \langle p, \nabla u \rangle_Y$.

A.2. Total Variation

In the discrete case, the total variation can be written by:

$$J(u) = \sum_{\substack{0 < i < M-1 \\ 0 < j < N-1}} |(\nabla u)_{i,j}| \tag{101}$$

$$= \sum_{\substack{0 < i < M-1 \\ 0 < j < N-1}} \sqrt{\left((\nabla u)^1_{i,j} \right)^2 + \left((\nabla u)^2_{i,j} \right)^2}. \tag{102}$$

However, J is a 1-homogeneous function ($J(\lambda u) = \lambda J(u)$); then if we apply the Legendre-Fenchel transform, we get:

$$J^*(v) = \sup_u \langle u, v \rangle_X - J(u) \tag{103}$$

with

$$\langle u, v \rangle_X = \sum_{i,j} u_{i,j} v_{i,j}, \tag{104}$$

where J^* is the characteristic function of the closed convex set K:

$$J^*(v) = \chi_K(v) = \begin{cases} 0 & \text{if} \quad v \in K \\ +\infty & \text{else} \end{cases}. \tag{105}$$

We have the property $J^{**} = J$.

In the continuous case (see the properties of the BV space), we have:

$$K = G_1 = \left\{ \text{div } \xi : \xi \in C_c^1(\Omega, \mathbb{R}^2); |\xi(x)| \leqslant 1, \forall x \in \Omega \right\} \tag{106}$$

then

$$J(u) = \sup_\xi \left\{ \int_\Omega u(x)\text{div } \xi(x)dx : \xi \in C_c^1(\Omega, \mathbb{R}^2); |\xi(x)| \leqslant 1, \forall x \in \Omega \right\}; \tag{107}$$

however, $\int_\Omega u(x)\text{div } \xi(x)dx = \langle u, \text{div } \xi \rangle_X$, then we can write:

$$J(u) = \sup_\xi \langle u, \text{div } \xi \rangle_X, \tag{108}$$

which is equivalent, if we write $v = \text{div } \xi$, to

$$J(u) = \sup_{v \in K} \langle u, v \rangle_X. \tag{109}$$

Now, we would like to have the same kind of expression for the discrete case. Chambolle proves the following lemma:

Lemma 1 *In the discrete case, we have:*

$$J(u) = \sup_{v \in G_1} \langle v, u \rangle, \tag{110}$$

$$where \quad G_1 = \{\text{div } p; p \in Y; |p_{i,j}| \leqslant 1\}. \tag{111}$$

Definition 8. Let us define the inner product over Y: let $p \in Y, q \in Y$ such that $p = \left(p^1, p^2\right)$ and $q = \left(q^1, q^2\right)$; then

$$\langle p, q \rangle_Y = \sum_{\substack{0 < i < M-1 \\ 0 < j < N-1}} (p_{i,j}^1 q_{i,j}^1 + p_{i,j}^2 q_{i,j}^2). \tag{112}$$

A.3. Chambolle's Projectors

We want to solve

$$\min_{u \in X} \frac{\|u - g\|^2}{2\lambda} + J(u) \tag{113}$$

with $g \in X$, $\lambda > 0$, $\|.\|$ is the euclidean norm defined by $\|u\|^2 = \langle u, u \rangle_X$.

If we apply Euler-Lagrange calculus to Eq.(113), we get

$$\frac{2(u-g)}{2\lambda} + \partial J(u) \ni 0 \tag{114}$$

$$\Longleftrightarrow u - g + \lambda \partial J(u) \ni 0, \tag{115}$$

where ∂J is the subdifferential of J defined by

$$w \in \partial J(u) \Longleftrightarrow J(v) \geqslant J(u) + \langle w, v - u \rangle_X \quad \forall v, \tag{116}$$

then Eq.(115) can be written as

$$\frac{g-u}{\lambda} \in \partial J(u) \tag{117}$$

$$\Longleftrightarrow \partial J^* \left(\frac{g-u}{\lambda} \right) \ni u \tag{118}$$

$$\Longleftrightarrow \frac{u}{\lambda} \in \frac{1}{\lambda} \partial J^* \left(\frac{g-u}{\lambda} \right) \tag{119}$$

$$\Longleftrightarrow \frac{g}{\lambda} \in \frac{g-u}{\lambda} + \frac{1}{\lambda} \partial J^* \left(\frac{g-u}{\lambda} \right). \tag{120}$$

If we reach a minimizer of

$$\frac{\left\| w - \left(\frac{g}{\lambda} \right) \right\|^2}{2} + \frac{1}{\lambda} J^*(w) \tag{121}$$

then by applying Euler-Lagrange calculus to Eq.(121), we get

$$w - \frac{g}{\lambda} + \frac{1}{\lambda} \partial J^*(w) \ni 0 \tag{122}$$

$$\Longleftrightarrow w + \frac{1}{\lambda} \partial J^*(w) \ni \frac{g}{\lambda}. \tag{123}$$

Thanks to Eq.(120), we see that

$$w = \frac{g-u}{\lambda} \tag{124}$$

is a minimizer of Eq.(121).

However as $J^*(w) = \chi_{G_1}(w)$ and if $w = P_{G_1} \left(\frac{g}{\lambda} \right)$ (the projector operator over G_1), then $J^*(w) = 0$ and $\left\| w - \frac{g}{\lambda} \right\|$ is minimum. We deduced that

$$P_{G_1} \left(\frac{g}{\lambda} \right) = \frac{g-u}{\lambda} \tag{125}$$

$$u = g - \lambda P_{G_1} \left(\frac{g}{\lambda} \right). \tag{126}$$

We have $P_{G_\lambda} \left(\frac{g}{\lambda} \right) = \lambda P_{G_1} \left(\frac{g}{\lambda} \right)$, then we have

$$u = g - P_{G_\lambda} \left(\frac{g}{\lambda} \right). \tag{127}$$

Now, we need to find how to calculate $P_{G_\lambda}(g)$. Chambolle gives the following result:

$$\text{computing } P_{G_\lambda}(g) \iff \min_{p \in Y} \left\{ \|\lambda \text{div}(p) - g\|^2; |p_{i,j}|^2 \leqslant 1 \quad \forall i,j \right\}. \tag{128}$$

The Karush-Kuhn-Tucker conditions showed the existence of a Lagrange multiplier $\alpha_{i,j} \geqslant 0$ associated with each constraint of Eq.(128) such that we have $\forall i,j$:

$$-\left(\nabla\left(\lambda \text{div}(p) - g\right)\right)_{i,j} + \alpha_{i,j} p_{i,j} = 0 \tag{129}$$

with

$$\alpha_{i,j} > 0 \quad \text{and} \quad |p_{i,j}| = 1 \tag{130}$$

$$\alpha_{i,j} = 0 \quad \text{and} \quad |p_{i,j}| < 1. \tag{131}$$

Then we can see that if $\alpha_{i,j} = 0$, then $\left(\nabla\left(\lambda \text{div}(p) - g\right)\right)_{i,j} = 0$; which is not an interesting case. For the case $\alpha_{i,j} \neq 0$:

$$\alpha_{i,j} p_{i,j} = \left(\nabla\left(\text{div}(p) - g\right)\right)_{i,j} \tag{132}$$

$$\Rightarrow |\alpha_{i,j}||p_{i,j}| = \left|\left(\nabla\left(\text{div}(p) - g\right)\right)_{i,j}\right|; \tag{133}$$

however, $|\alpha_{i,j}| = \alpha_{i,j}$ because $\alpha_{i,j} > 0$ and $|p_{i,j}| = 1$; then

$$\alpha_{i,j} = \left|\left(\nabla\left(\text{div}(p) - g\right)\right)_{i,j}\right|. \tag{134}$$

Now, if we use a gradient steepest descent method with $\tau > 0$; $p^0 = 0$; $n \geqslant 0$, we get

$$p_{i,j}^{n+1} = p_{i,j}^n + \tau\left[\left(\nabla\left(\text{div}(p^n) - \frac{g}{\lambda}\right)\right)_{i,j} - \left|\left(\nabla\left(\text{div}(p^n) - \frac{g}{\lambda}\right)\right)_{i,j}\right| p_{i,j}^{n+1}\right]. \tag{135}$$

Finally, we get the following iterative formulation:

$$p_{i,j}^{n+1} = \frac{p_{i,j}^n + \tau\left(\nabla\left(\text{div}(p^n) - \frac{g}{\lambda}\right)\right)_{i,j}}{1 + \tau\left|\left(\nabla\left(\text{div}(p^n) - \frac{g}{\lambda}\right)\right)_{i,j}\right|}. \tag{136}$$

Chambolle proves the following important theorem.

Theorem 3 *If $\tau < \frac{1}{8}$ then $\lambda \text{div}(p^n)$ converges to $P_{G_\lambda}(g)$ when $n \to +\infty$.*

In pratice, we note that the choice $n = 20$ is sufficient to reach the wanted convergence.

A.4. Extension

The previous result can be extended to the case of $BV - \mathcal{H}$ functional where $\mathcal{H}$ is a Hilbert space such that there exists a linear positive symmetric operator K that defines the following norm over $\mathcal{H}$:

$$\langle f, g \rangle_{\mathcal{H}} = \langle f, Kg \rangle_{L^2} \tag{137}$$

Then, if we want to minimize

$$J(u) + \frac{\lambda}{2}\|f - u\|_{\mathcal{H}}^2, \tag{138}$$

we can use the following modified Chambolle projector:

$$p_{i,j}^{n+1} = \frac{p_{i,j}^n + \tau \left(\nabla \left(K^{-1} \mathrm{div} \left(p^n \right) - \frac{g}{\lambda} \right) \right)_{i,j}}{1 + \tau \left| \left(\nabla \left(K^{-1} \mathrm{div} \left(p^n \right) - \frac{g}{\lambda} \right) \right)_{i,j} \right|}. \tag{139}$$

And the corresponding convergence theorem is shown below.

Theorem 4 *If $\tau < \frac{1}{8\|K^{-1}\|_{L^2}}$, then $\frac{1}{\lambda} K^{-1} \mathrm{div} \left(p^n \right)$ converges to $\hat{v}$ when $n \to +\infty$ and $f - \frac{1}{\lambda} K^{-1} \mathrm{div} \left(p^n \right) \to \hat{u}$ where $\hat{u}$ is the minimizer of Eq.(138).*

A special case is for $K = -\Delta^{-1}$, which corresponds to the Sobolev case $\mathcal{H} = H^{-1}$.

References

Adams, R., 1975. Sobolev spaces. Academic Press.

Aujol, J., 2004. Contribution à l'analyse de textures en traitement d'images par méthodes variationnelles et équations aux dérivées partielles. Ph.D. thesis, University of Nice Sophia Antipolis.

Aujol, J., Aubert, G., Blanc-Féraud, L., Chambolle, A., 2003. Decomposing an image. application to textured images and SAR images. Tech. rep., University of Nice Sophia-Antipolis.

Aujol, J., Chambolle, A., 2005. Dual norms and image decomposition models. International Journal of Computer Vision 63 (1), 85–104.

Aujol, J., Gilboa, G., 2006. Constrained and snr-based solutions for tv-hilbert space image denoising. Journal of Mathematical Imaging and Vision 26 (1-2), 217–237.

Aujol, J., Gilboa, G., Chan, T., Osher, S., 2006. Structure-texture image decomposition-modeling, algorithms and parameter selection. International Journal of Computer Vision 67 (1), 111–136.

Bamberger, R., Smith, M., 1992. A filter bank for the directional decomposition of images: Theory and design. IEEE Trans. Signal Processing 40 (4), 882–893.

Burt, P., Adelson, E., 1983. The laplacian pyramid as a compact image code. IEEE Trans. Commun. 31 (4), 532–540.

Candès, E., Donoho, D., 1999. Curvelets: A surprisingly effective nonadaptive representation of objects with edges. Tech. rep., Department of Statistics, Stanford University.

Candès, E., 1998. Ridgelets: Theory and applications. Ph.D. thesis, Department of Statistics, Stanford University.

Candès, E., Demanet, L., Donoho, D., Ying, L., 2005. Fast discrete curvelet transforms. Multiscale Modeling and Simulation 5, 861–899.

Chambolle, A., mars 2004. An algorithm for total variation minimization and applications. Journal of Mathematical Imaging and Vision 20 (1-2), 89–97.

Chambolle, A., DeVore, R., Lee, N., Lucier, B., 1998. Nonlinear wavelet image processing: variational problems, compression and noise removal through wavelet shrinkage. IEEE Trans. on Image Processing 7, 319–335.

Daubechies, I., 1992. Ten lectures on wavelets. Society for Industrial and Applied Mathematics.

Do, M., 2001. Directional multiresolution image representations. Ph.D. thesis, Department of Communication Systems, Swiss Federal Institute of Technology Lausanne.

Do, M., 2003. Contourlets and sparse image representations. SPIE conference on Wavelet Applications in Signal and Image Processing X, San Diego, USA.

Do, M., Vetterli, M., 2001. Pyramidal directional filter banks and curvelets. IEEE International Conference on Image Processing (ICIP), Thessaloniki, Greece.

Do, M., Vetterli, M., 2002. Contourlets: A directional multiresolution image representation. IEEE International Conference on Image Processing (ICIP), Rochester.

Do, M., Vetterli, M., 2003a. The contourlet transform: an efficient directional multiresolution image representation. IEEE Trans. Image Processing 14 (12), 2091–2106.

Do, M., Vetterli, M., 2003b. Framing pyramids. IEEE Trans. Signal Processing 51, 2329–2342.

Donoho, D., Duncan, M., 1999. Digital curvelet transform: strategy, implementation and experiments. Tech. rep., Department of Statistics, Stanford University.

Gilboa, G., Zeevi, Y., Sochen, N., 2003. Texture preserving variational denoising using an adaptive fidelity term. Proceedings of VLSM, pp. 137–144.

Gilles, J., 2007a. Choix d'un espace de représentation image adpaté à la détection de réseaux routiers. Traitement et Analyse de l'Information: Méthode et Application (TAIMA) Workshop, Hammamet, Tunisia.

Gilles, J., 2007b. Noisy image decomposition: a new structure, texture and noise model based on local adaptivity. Journal of Mathematical Imaging and Vision 28 (3), 285–295.

Haddad, A., 2005. Méthodes variationnelles en traitement d'image. Ph.D. thesis, Ecole Normale Supérieure de Cachan, France.

Härdle, W., Kerkyacharian, G., Picard, D., Tsybakov, A., 1997. Wavelets, approximation and statistical applications, proceeding of Paris-Berlin seminar.
URL http://www.quantlet.com/mdstat/scripts/wav/html/index.html

J. Bobin, J.-L. Starck, M. F., Moudden, Y., 2007. Sparsity, morphological diversity and blind source separation. IEEE Trans. on Image Processing 16 (11), 2662–2674.

J. Bobin, J.-L. Starck J. Fadili, Y. M., Donoho, D., 2007. Morphological component analysis: an adaptative thresholding strategy. IEEE Trans. on Image Processing 16 (11), 2675–2681.

J.B. Garnett, P. Jones, M. T., Vese, L., 2005. Modeling oscillatory components with the homogeneous spaces $\dot{BMO}^{-\alpha}$ and $\dot{W}^{-\alpha,p}$. Tech. rep., UCLA CAM Report 07-21.

Mallat, S., 1999. A wavelet tour of signal processing. Academic Press.

Meyer, Y., 1993. Wavelets: Algorithms and Applications. Society for Industrial and Applied Mathematics.

Meyer, Y., 2001. Oscillating patterns in image processing and in some nonlinear evolution equations. The Fifteenth Dean Jacquelines B. Lewis Memorial Lectures, American Mathematical Society.

Osher, S., Sole, A., Vese, L., 2002. Image decomposition and restoration using total variation minimization and the H^{-1} norm. Multiscale Modeling and Simulation: A SIAM Interdisciplinary Journal 1 (3), 349–370.

Po, D., Do, M., 2006. Directional multiscale modeling of images using the contourlet transform. IEEE Trans. Image Processing 15 (6), 1610–1620.

Rudin, L., Osher, S., Fatemi, E., 1992. Nonlinear total variation based noise removal algorithms. Physica D 60, 259–268.

Triebel, H., 1992. Theory of function spaces II. Birkhäuser Basel.

Triet, M., Vese, L., 2005. Image decomposition using total variation and $div(BMO)$. Multiscale Modeling and Simulation, SIAM Interdisciplinary Journal 4 (2), 390–423.

Vese, L., 1996. Variational methods and partial differential equations for image analysis and curve evolution. Ph.D. thesis, University of Nice - Sophia Antipolis, France.

Vese, L., Osher, S., 2002. Modeling textures with total variation minimization and oscillating patterns in image processing. Journal of Scientific Computing 19 (1-3), 553–572.

Vidakovic, B., Mueller, P., 1991. Wavelets for kids. http://www.isye.gatech.edu/~brani/wp/kidsA.ps, cours d'introduction aux ondelettes.